NOVA SCHOOL OF
SCIENCE & TECHNOLOGY

DEPARTAMENT OFMATERIALS SCIENCE

Mariana Monteiro Duarte

BSc in Materials Engineering

# Additive Fabrication of Metallic Anepectic meshes

MASTER IN MATERIALS ENGINEERING

NOVA University Lisbon

September, 2022

NOVA SCHOOL OF
SCIENCE & TECHNOLOGY

DEPARTAMENT OF MATERIALS SCIENCE

---

# Additive Fabrication of Metallic Anepectic meshes

**MARIANA MONTEIRO DUARTE**
BSc in Materials Engineering

**Adviser:** Alexandre José da Costa Velhinho
*Assistant Professor, NOVA University Lisbon*
**Co-advisers:** Rodolfo Lisboa Batalha
Senior Researcher, ISQ (Institute for Welding and Quality)

**Examination Committee:**

**Chair:** Prof. Dr. Rui Silva,
*Fullt Professor, NOVA University Lisbon*
**Rapporteur:** Prof. Dr. João Pedro Oliveira,
*Assistant Professor, NOVA University Lisbon*
**Adviser:** Prof. Dr. Alexandre José da Costa Velhinho,
*Assistant Professor, NOVA University Lisbon*

MASTER IN MATERIALS ENGINEERING

NOVA University Lisbon
September, 2022

**Additive Fabrication of Metallic Anepectic Meshes**

# ACKNOWLEDGMENTS

For starters, I want to acknowledge my advisors, Professor Dr. Alexandre Velhinho and Dr. Rodolfo L. Batalha. To Professor Dr. Alexandre Velhinho, I want to thank for the support, guidance, and availability demonstrated to help, for all the knowledge transmitted during these months, and for recommending me to choose this thesis that despite being challenging, was extremely exciting and rewarding to develop. To Dr. Rodolfo Batalha I am grateful for the availability to help me whenever and for whatever was needed, as well as for the good moments spent at ISQ. I also want to acknowledge Professor Dr. João Paulo Borges for all the support and collaboration given during the whole process, giving an outside perspective on the topic.

I want to thank my faculty, especially the Department of Material Sciences for the support during the development of this project, and for all the dedication during my academic path. More specifically, I am also very grateful to João Cardoso for all the time spent helping me, answering my tons of questions, and guiding me. I also want to acknowledge ISQ (*Instituto de Soldadura e Qualidade*) for giving me the possibility to develop my thesis, allowing me to grow, and learn more about additive manufacturing and welding.

To my mom, Paula Duarte I want to give my dearest thank you, for being my biggest support during my whole education (and life, obviously), and especially during these last extra hard years. Thank you for all the resources and feedback provided so that I could grow into the person that I am today.

To my ISQ companions Francisca Salgueiro, Iuri Vilhena, André Carvalho, and Francisco Feliciano I would like to thank you all for being there, helping, giving tips, feedback, and very helpful input, as well for the good times, laughing and games that we shared in our "now not so empty" office.

These 5 years and two different courses allowed some very special people to come into my life, whom I am very proud to call friends. To (Maria) Inês Costa, João Leal Oliveira, Carlos Duarte, Ivan Santos, André Pequito Rocha, Bianca Sousa, Daniel Rodrigues, Pedro Rebola and Afonso Azevedo, thank you for all the support, laughs, good memories, and late-night study sessions. I will carry you all in my heart.

“I go to seek a Great Perhaps.”
(François Rabelais).

# ABSTRACT

Taking advantage of additive manufacturing capabilities, a two-dimensional re-entrant star-shaped metal structure was successfully fabricated. Seeking to achieve anepectic behaviour, as it can only be attained when the two constituent materials have similar but different stiffness values and widely different CTE, two materials were selected, namely Inconel 625 and AlSi10Mg.

A parameter optimization was performed for the equipment and the selected materials. Using these parameters, two different types of single material meshes, with a thickness of 1mm and 0.5mm respectively, were printed and mechanically tested, successfully exhibiting auxetic behaviour, proving that natural auxeticity can also be achieved with metallic meshes.

With a view to also achieve the anepectic behaviour, the compatibility and interconnection of the selected materials were also studied, using for that purpose printed bimetallic meshes. Recurring to optical microscopy and scanning electron microscopy, the interface between the two materials was studied. When the printing process started by AlSi10Mg followed by Inconel 625 interesting results were obtained as it exhibited an small interdiffusion area, however further studies are recommended. In order to analyse the possibility to achieve anepectic behaviour in metallic meshes, more studies are necessary.

**Keywords:** Anepectic, Auxetic, Negative coefficient of thermal expansion, Negative Poisson's ratio, Additive manufacturing, Metallic structures

# RESUMO

Tirando partido das capacidades da fabricação aditiva, foi produzida com sucesso uma estrutura metálica bidimensional reentrante em forma de estrela. Procurando alcançar um comportamento anepéctico, como este só pode ser observado quando os dois materiais constituintes apresentam valores de rigidez semelhantes, mas CTE muito diferentes, dois materiais foram selecionados, nomeadamente o Inconel 625 e o AlSi10Mg.

Foi realizada uma otimização de parâmetros para o equipamento e para os materiais escolhidos. Utilizando estes parâmetros, foram impressos e testados mecanicamente dois tipos de malha de um único material, com uma espessura de 1mm e 0,5mm respetivamente, exibindo com sucesso o comportamento auxético, provando que a auxeticidade natural também pode ser verificada com malhas metálicas.

Com vista a alcançar também o comportamento anepéctico, foi também estudada a compatibilidade e interligação dos materiais selecionados, utilizando para o efeito malhas bimetálicas impressas. Utilizando microscopia ótica e microscopia eletrónica de varrimento, a interface entre eles foi estudada. Ao iniciar o processo de impressão pelo AlSi10Mg, seguida pelo Inconel 625, foram obtidos resultados interessantes, contudo recomenda-se a realização de mais estudos. A fim de analisar a possibilidade de se obter um comportamento anepéctico, são ainda necessários mais estudos.

**Palavras-chave:** Anepéctico, Auxético, Coeficiente de expansão térmica negativo, Coeficiente de Poisson Negativo, Fabricação aditiva, Estruturas metálicas

# CONTENTS

# LIST OF FIGURES

# LIST OF TABLES

# GLOSSARY

| | |
|---|---|
| **Exposure time** | Amount of time the beam stays at one spot at the time. |
| **Hatching Distance** | Distance between columns made of fused points |
| **Point distance** | When the beam is in pulsed mode, it is the distance between the centers of two consecutive points. |

# ACRONYMS

| | |
|---|---|
| **2D** | Two Dimensional. |
| **3D** | Three Dimensional. |
| **AM** | Additive Manufacturing. |
| **CTE** | Coefficient of Thermal Expansion. |
| **DoE** | Design of Experiments |
| **E** | Young modulus |
| **ISQ** | *Instituto de Soldadura e Qualidade* (Quality and Welding Institute) |
| **L-DED** | Laser-based Directed Energy Deposition. |
| **L-PBF** | Laser Powder Bed Fusion. |
| **NPR** | Negative Poisson Ratio. |
| **NTE** | Negative Thermal Expansion. |
| **PR** | Poisson Ratio. |
| **RBV** | Reduced Build Volume |
| **SS** | Stainless Steel |
| **WAAM** | Wire Arc Additive Manufacturing. |

# SYMBOLS

| | |
|---|---|
| **%** | Percentage |
| **µm** | Micrometers |
| **GPa** | Giga Pascal |
| **L** | Liters |
| **ºC** | Degrees Celsius |
| **ppm** | parts per million |
| **W** | Watts |
| $\boldsymbol{\theta}$ | The greek letter theta |

# MOTIVATION AND OBJECTIVES

There has been an increase of interest regarding metamaterials that present a combination of different coefficients or behaviours. Anepectic metamaterials are capable of demonstrate a negative Poisson's ratio (NPR) in conjunction with a negative thermal expansion (NTE) presenting a relative dimensional insensitivity to mechanical and thermal stimuli.

With the successful development of 2D polymeric anepectic metamaterials with a re-entrant star shaped geometry mesh, metallic materials have been becoming integrated as in polymeric/metallic meshes, also successfully achieving the anepectic. Thus, based on the re-entrant star shaped meshes previously studied, the present dissertation aims do manufacture the first full metallic anepectic mesh, recurring to the advantages of additive manufacturing using metal powders as starting materials

# 1

# INTRODUCTION

Metamaterials are materials engineered to present properties and functionalities hard to achieve in natural materials. According to their functionalities, they can be classified into four different categories: electromagnetic, acoustic, thermal, or mechanical metamaterials [1], [2]. This work will focus on the latter.

Mechanical metamaterials present tuneable mechanical properties derived from their architected structures with precise shape, geometry, size, and orientation [3], [4]. These metamaterials, which often show negative parameters, such as a negative Poisson's ratio (NPR), negative thermal expansion (NTE), or negative compressibility, present counter-intuitive behaviour, thus offering a broader range of opportunities to design innovative structures [5].

The mechanical metamaterials present several potential applications, examples being in vehicles' vibration protection systems through its negative stiffness, in deep ocean applications, where compression needs to be avoided, and in medical applications such as in stents due to the ability to expand and compress in both directions simultaneously [1], [6].

With the development of additive manufacturing (AM) and its ability to produce highly intricate and complex structures, the production of metamaterials has become feasible. This has been attracting interest to metamaterials from multiple areas that require precise control of geometry and internal structure during production, features that are hard to achieve with more conventional manufacturing techniques [2], [7], [8].

## 1.1 Negative Poisson's ratio

The Poisson's ratio (PR) is a dimensionless constant that measures the ratio between the resulting transverse strain and the longitudinal strain of a body when stress is applied along that longitudinal direction [9]. Theoretically, for materials in bulk this ratio ranges from -1 to 0.5, with most metals, polymers, and ceramics presenting values between 0.25-0.35. Specifically for those cases, where the Poisson's ratio is null or negative, the term 'auxetic' was introduced by Evans *et al*. [1], [10].

Most known auxetic materials whether were discovered, fabricated, or synthesised, and their macroscopic behaviour is mainly due to their structure design rather than their composition, as happens with natural materials. The auxeticity provides improved properties compared to conventional materials, such as higher resistance to shear, increased fracture toughness, enhanced indentation resistance, a superior energy absorption performance, and a variable permeability [11]–[14].

One of the first auxetic structures was presented by Lakes in 1987 as a polyester foam with a re-entrant geometry [15]. Since then, several structures have been studied that bend, fold, or rotate upon themselves when compressed [16]. Whether 2D or 3D, these structures can be grouped into five categories based on their geometry: re-entrant, chiral, rotating, crumpled sheets, and perforated sheets, as represented in Figure 1.1 [16].

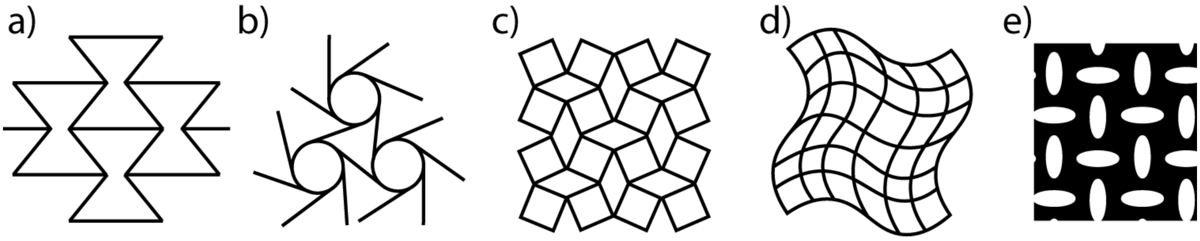

Figure 1.1 Schematics representing the five categories of auxetic structures. a) re-entrant; b) chiral; c) rotating; d) crumpled sheets; e) perforated sheets. Adapted [16]

Despite being associated with engineered materials, auxeticity exists in some naturally occurring materials such as in the mineral rutherfordine [17], in 2D black phosphorous [18], in iron pyrite, or even in cat skin or in cancellous bone from the proximal tibial epiphysis [11].

In terms of applications, negative Poisson ratio (NPR), materials have a lot of potential. In biomedicine, they may be used for stents, by taking advantage of auxetics' ability to expand, allowing them to present a good fixation [19]. It may be used for artificial blood vessels, given that they increase the vessel's thickness when a pulse of blood flows [20]. Another example are in defense equipments, such as bulletproof vests or other protective clothing, or even appliqué armour for vehicles and buildings, since auxetics can dissipate efficiently a great amount of energy [20]. NPR materials may also be used for wearable electronics such as stretchable strain sensors, as they depend greatly on the material mechanical properties under deformation [11], [18], [21].

## 1.2 Negative thermal expansion

The coefficient of thermal expansion (CTE) describes the volume variation of a given material when submitted to a different temperature [22]. Most solids expand upon heating as the interatomic bonds increase their length [12], [23]. However, although rare, some natural materials present a negative thermal expansion coefficient, expanding when cooled [23]. In fact, this behaviour is not due to the shortening of bonds with the increasing temperature, but due to other mechanisms, such as displacive phase transition, ferroelectrostriction, and magnetostriction [24]–[26].

The most known material with a negative thermal expansion coefficient is water when transitioning from liquid to solid. However, there are other natural NTE materials, such as perovskite ($CaTiO_3$) and zirconium tungstate ($ZrW_2O_8$) [24], [26].

The unusual behaviour of NTE materials has increased its interest for several applications similarly to composites, in which the combination of different materials allows the CTE tailoring. This property is quite critical in precision devices, as on high-precision optics or antennas on satellites and space telescope mirrors, since thermal expansion affects their accuracy [1], [25], [27]. Areas such as electronics also benefits from NTE to increase devices efficiency. Besides that, there are dental fillings and other domains where in-service temperature fluctuations might cause fatigue and cracking [24]–[28].

## 1.3 Anepectic meshes

For the cases where metamaterials present simultaneously NPR and NTE, J. Raminhos *et al.* proposed the designation "anepectic", based on the Greek word for expansion (*επέκταση - epéktasi*) [3]. Those authors fabricated the first anepectic meshes, as previous studies had not succeeded to physically produce these structures [3]. The concept for this specific metamaterial was firstly studied by L. Ai *et al*. [29].

Resorting to a combination of a star-shaped re-entrant structure and a bi-material lattice design, L. Ai *et al.* were able to study a structure that allows for the creation of an anepectic mesh, using appropriated geometrical parameters and material combinations [29]. To present anepectic behaviour, the designed mesh must meet one requirement: the constitutional materials need to have similar yet different stiffness, but widely different CTE [1], [30].

The mesh design used in the present work will be the same as the one used by J. Raminhos *et al*. and as first introduced by L. Ai *et al*.. The unit cell of the mesh structure is presented in Figure 1.2, and it can be characterized by "a", "b" and "θ”. This structure is characterized by its inherent auxeticity and has the great advantage of not involving pins, adhesives, or any welded joints [3], [29].

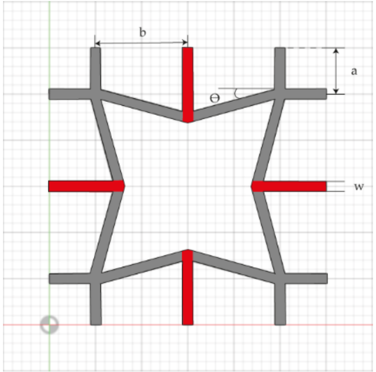

Figure 1.2 Unit cell for a star-shaped re-entrant structure. (Adapted from [3])

As mentioned before, J. Raminhos *et al.* designed three different star-shaped re-entrant meshes only varying the angle parameter θ from 15 to 35 degrees. They were printed and tested, and all of them presented the desired anepectic behaviour. To produce the first anepectic meshes, they used several combinations of four different constituent polymers that present a positive CTE [3].

After L. Ai *et al.*, other authors designed meshes that should present anepectic behaviour. X. Li *et al.* [31] designed and 3D printed a star-squared structure mesh, using a layer-by-layer deposition of resin and achieved anepectic behaviour [31]. N. Xu *et al.* [32], were able to study a novel 3D structure by changing the material combination of the inner and outer cell walls, achieving the anepectic behaviour and with enhanced NPR effect [32].

I. Marcelino [33] produced bi-material re-entrant meshes with a ABS polymer, in the passive part (blue beams in Figure 1.2), and a shape memory nickel-titanium alloy in the active part of the mesh (red beams in Figure 1.2). In the work presented, anepectic behaviour was observed only in five out of seven composite meshes due to the curved wire configuration [33]. J. Parada [12] also successfully produced polymeric anepectic meshes allied with copper and with steel wires that can induce a controlled temperature variation by resistive heating. It was achieved a 5% deformation of the initial form with a 4 A current, proving its feasibility in applications where small and controlled deformations are required [12].

## 1.4 Additive manufacturing

Additive manufacturing ability to produce near-net shape products, is transforming the manufacturing industry, as it can fabricate products with complex geometries and reducing the generated waste. It allows the fabrication layer-by-layer leading to the ability to produce quite intricate designs with remarkable properties [2], [34], [35]

AM technologies can be categorized into three types, according to the raw material: liquid, filament or powder, and they can be applied to metals, polymers and ceramics [2]. In the present work, we will focus on metals.

AM may also be used to print multi-metal materials, recurring to techniques such as wire-arc additive manufacturing (WAAM), laser-based directed energy deposition (L-DED), and laser-powder bed fusion (L-PBF) [36], which will be used to produce the metallic meshes in this work.

L-PBF working principle consists of a re-coater that spreads a homogeneous thin layer of powder with a specific height. Then, a laser beam selectively melts the powder according to a 3D design. After the first layer, where the powder is fused to the build plate, the process is repeated until the desired structure is completed. In the chamber, usually argon or nitrogen are used as a protective atmosphere [37], [38].

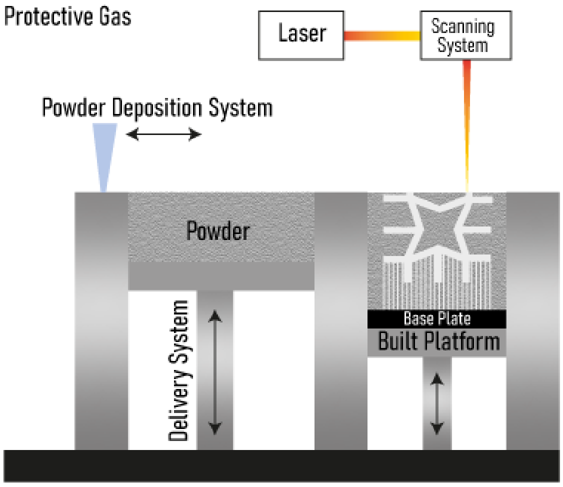

Figure 1.3 L-PBF working principle

The powder used is one of the key components of L-PBF printing process, as its properties have an important impact on the final product. Several characteristics as the thermal, metallurgical, mechanical and rheological characteristics, and the powder's chemical composition, more specifically a spherical morphology, high packing density, a good flowability and an even spreading are crucial for the process to occur In the best conditions [35], [39]. Depending on the type of powder used, the build plate must be compatible to the material and it must be cleaned after use by specific techniques such as grinding, milling or turning [40].

However, L-PBF presents some challenges when used for multi-material printing. In the present work, the possibility of several defects increases since each material composition may require an optimal process parameter [36]. Therefore, the main goal of this work is the manufacturing of an anepectic structure by L-PBF recurring to metallic materials.

# 2

# MATERIALS AND METHODS

As previously mentioned, the choice of the materials must be done very carefully, since the constitutional materials of the mesh need to have similar, yet different stiffness but widely different CTE in order to present anepectic behaviour. Considering Figure 1.2, the grey beams must be made by a material with a lower CTE and higher E, while the red beams must present a high CTE and lower E. The materials considered are presented in Table 2.1, with their correspondent Young's modulus and CTE.

Table 2.1 List of powders considered to choose.

| ***Material*** | **Temperature interval for values presented [°C]** | **CTE [ppm/°C]** | **Young's Modulus [GPa]** | **Reference** |
|---|---|---|---|---|
| *Invar* | 20 to 200 | 1.1 to 2.5 | 135 to 144 | [29] |
| *Inconel 625* | 20 to 200 | 12.8 | 195 to 215 [1] | [41] |
| *SS 316L* | 0 to 100 | 16.0 | 193 to 201 [1] | [42] |
| *AlSi10Mg* | 0 to 100 | 20.0 to 21.0 | 48 to 80 [1] | [43] |
| *AA 2319* | 20 to 200 | 23.4 | 72 | [44]–[46] |
| *AA 7075* | 20 to 200 | 23.0 to 24.3 | 66 to 71 | [29] |

*[1] Values obtained for additively manufactured components, without thermal treatment and in the horizontal direction (XY)*

*Note: The values presented stand for the material in bulk.*

Considering the data and rules to anepectic behaviour, the best combinations of materials are presented in Table 2.2. The 3rd combination was selected since was the only combination of materials that were simultaneously available at ISQ.

Table 2.2 Combinations of the materials that respect the condition for anepectic behaviour.

| | | |
|---|---|---|
| *1.* | Invar | Grey beam |
| | AA 2319 | Red beam |
| *2.* | Invar | Grey beam |
| | AlSi10Mg | Red beam |
| *3.* | Inconel 625 | Grey beam |
| | AlSi10Mg | Red beam |

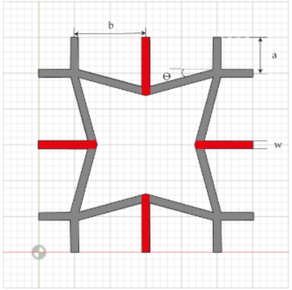

## 2.1 AlSi10Mg

AlSi10Mg is well known among aluminium alloys for its weldability [47], and when it is processed with L-PBF presents low weight, high specific strength, stiffness, low thermal expansion coefficient, and corrosion resistance with a flexible post-processing [48]–[50]. Because of these properties, it has several industrial applications such as automotive, aerospace, and electronics [47], [49]. At the moment, AlSi10Mg has been successfully used for high-performance parts, however, during the production, when it is submitted to high temperatures and cooling rates, some defects inevitably appear such as pores or cracks [47].

The AlSi10Mg powder used for the present work was sourced from Renishaw (United Kingdom), with the specific lot 21388422720001, and its chemical composition is presented in Table 2.3, as specified by the supplier. The particle size is comprised in the 20 to 63µm range, also according to the supplier.

Table 2.3 Chemical Composition of AlSi10Mg, according to the supplier.

| *Element* | *W/w %* | *Element* | *W/w%* |
|---|---|---|---|
| *Aluminium* | Balance | *Zn* | 0.10 Max. |
| *Si* | 9.00 to 11.00 | *Cu* | 0.05 Max. |
| *Mg* | 0.25 to 0.45 | *Ni* | 0.05 Max. |
| *Fe* | 0.25 Max. | *Pb* | 0.02 Max. |
| *N* | 0.20 Max. | *Sn* | 0.02 Max. |
| *O* | 0.20 Max. | *Others ind* | 0.05 Max. |
| *Ti* | 0.15 Max. | *Others all* | 0.05 Max. |
| *Mn* | 0.10 Max. | | |

## 2.2 Inconel 625

For the passive part of the structure, represented in grey on Figure 1.2, a nickel-based superalloy was selected. By the presence of Nb and Mo in its Ni-Cr matrix, Inconel 625 (IN625) presents high yield and fatigue strength as well as an excellent corrosion resistance and good weldability [48], [51]. Allied with its low thermal conductivity, this alloy is considered to have a difficult machinability, making it a good material to process via AM [51], [52]. IN625 is suitable for a wide range of applications in aerospace industries, defence, and energy such as nuclear, oil and gas [48], [51].

The IN625 powder used for the present work were sourced from Renishaw (South Wales), with the specific lot 0000139398, and its chemical composition is presented in Table 2.3, as specified by the supplier. According to the supplier, the particle size is comprised in the interval between 15 and 45 µm.

Table 2.4 Chemical Composition of Inconel 625, according to the supplier.

| *Element* | *W/w %* | *Element* | *W/w%* |
|---|---|---|---|
| *Ni* | Balance | *Ti* | 0.100 Max. |
| *Cr* | 20.000 to 23.000 | *Al* | 0.050 Max. |
| *Mo* | 8.000 to 10.000 | *P* | 0.150 Max. |
| *Fe* | 5.000 Max. | *S* | 0.150 Max. |
| *Nb+Ta* | 3.150 to 4.150 | *C* | 0.100 Max. |
| *Co* | 1.000 Max. | *O* | 0.030 Max. |
| *Si* | 0.500 Max. | *N* | 0.015 Max. |
| *Mn* | 0.500 Max. | *Others all* | 0.050 Max. |

## 2.3 Laser Powder Bed Fusion

The laser-powder bed fusion (L-PBF) system available at ISQ is the Renishaw RenAM 500S Flex. This equipment presents a single (S) 500W laser of ytterbium fiber with wavelength of 1070 nm and a spot size of 80 µm [40]. The build envelope of the equipment is 250 mm x 250 mm x 350 mm which during printing is under an argon atmosphere [40]. The system available is flexible to facilitate the process of powder changing and can be converted to an on-system powder sieving and recycling, increasing productivity on the same qualified machine.

For the production of smaller builds, the build envelope, may be downsized to a reduced build volume, RBV, with the maximum volume of 78 mm x 78 mm x 50 mm and using between 0,25L to 0.75L of powder [53].This tool enables users to quickly change between materials, as it is independent from the machines' powder handling system, using a significantly less amount of material [53].

In order to facilitate the removal of the meshes impressed, with a minimal post processing, the prints in the present work are done recurring to support structures. These structures are a system of thin walls, pins and cellular structures used to elevate the build for a simpler removal, to improve heat dissipation, and to prevent the deformation of the part [35], [38]. For the insertion of these supports, there are several software’s that allow the automatic generation of supports in the desired structure [35]. For the current work, the supports were automatic generated and using the program QuantAM from Renishaw [54].

Figure 2.1 Renishaw RenAM 500S Flex available at ISQ.

## 2.4 Design of Experiments

Design of Experiments is the method selected for the identification of the best printing parameters in L-PBF. The method consists of the realization of systematic tests, called experiments, that allow the identification of factors that have a preponderant effect on a response [55], [56]. When the factors are identified the goal of DoE is optimize the response variable.

A DoE is composed by seven steps. First step is to define the target of the design taking into account some questions and problems to be addressed. Second step is the identification of the response(s) variable(s), such as the roughness, thickness, continuity, etc. In the third step, the choice of factors, levels, and the range of each is made. Regarding L-PBF, as an example of this step, a factor like power, may have three levels such as 100 Watts, 200 W, and 300W. Step four consists of the selection of the number of replicas, and the order for the experiments to run. Step five is the realization of the experiment, and step six is the statistical analysis of the data. Lastly, the seventh step is conclusions and recommendations [56].

# 3

# RESULTS AND DISCUSSION

## 3.1 Powder's characterization

### AlSi10Mg

The average particle size was measured recurring to a granulometric analysis, with a powder sieve BA200N from CISA, presented in Annex A. The powders were sieved for 15 minutes and recurring to 4 different mesh sizes, specifically 63µm, 45µm, 38µm and 20µm. The results of this analysis are presented Figure 3.1, where it is possible to infer that 53,61% of the particles are comprised in the particle size interval from 45µm to 63µm. According to the supplier, the powders particle size is comprehended between 20µm to 63µm, since 62,78% is inserted in that interval, the supplier's interval can be confirmed. The powders distribution can be characterized by a D10 and D50 of 45.276µm and 58.707µm, respectively. The 36% with a size higher than 63µm may be caused due to powder's agglomeration as a response to the rooms' humidity. In Annex B it is available the tables with the data used.

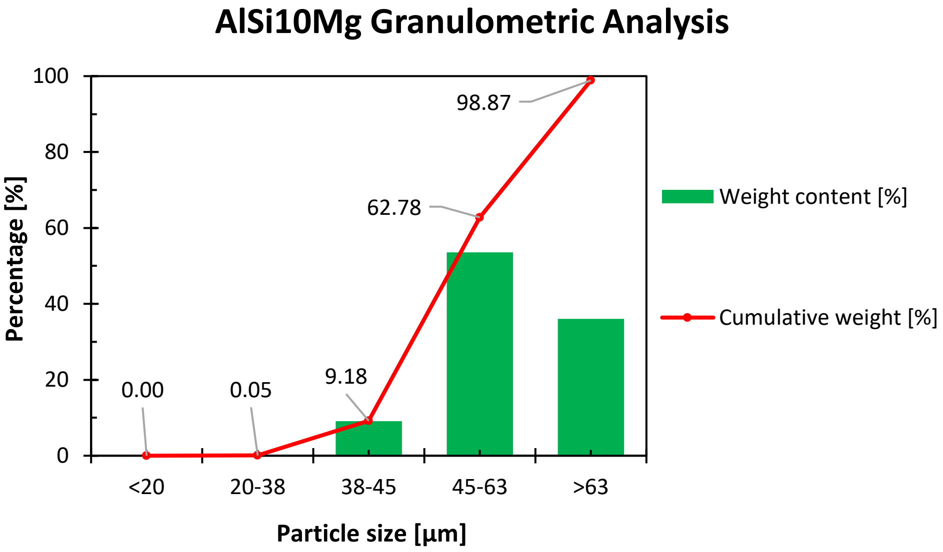

Figure 3.1 Granulometric analysis of the AlSi10Mg powder used.

The morphology was observed by embedding a small amount of powder in Epoxy resin and post processed by polishing its surface with an EcoMet30 from BUEHLER with the recipe for metallographic preparation of Al-based alloys (presented in Annex A), as presented in Figure 3.2. The sample was observed recurring to a Zeiss optical microscope with an Infinity 2 digital camera (presented in Annex

A), obtaining the pictures presented in Figure 3.3. In these photos, we can affirm that the powder has a spherical morphology, which is ideal for L-PBF printing.

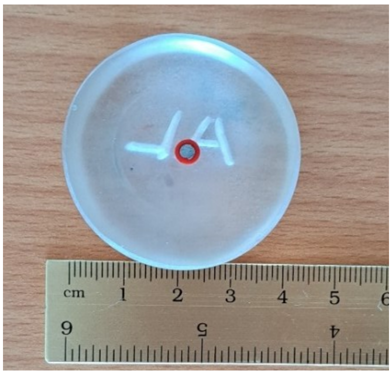

Figure 3.2 AlSi10Mg powder embedded in polished Epoxy resin.

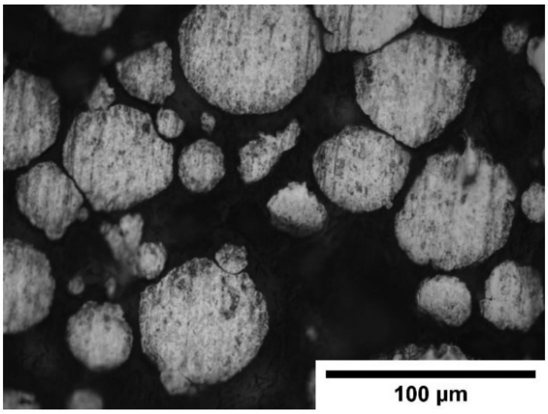

Figure 3.3 Cross-section of the AlSi10Mg powder obtain with an optical microscope, to observe its morphology.

## Inconel 625

As previously done for the AlSi10Mg powder, the average particle size was measured recurring to a granulometric analysis. The results of the analysis are presented in Figure 3.4, where we can infer that most of the particles have sizes between 20µm and 63µm, coincident with the particle size interval of 20 to 63 given by the supplier. The powders distribution can be characterized by a D10, D50 and D90 of 33.919µm, 52.458µm and 61.645µm, respectively, confirming the interval given by the supplier, since D90 is below 63µm.

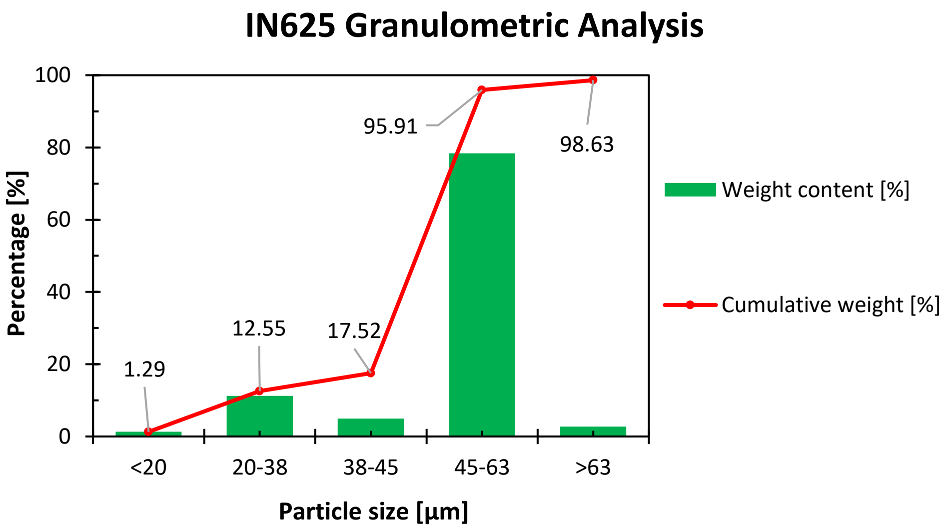

Figure 3.4 Granulometric analysis of the Inconel 625 powder used.

In similarity with what has been done with AlSi10Mg, for IN625 morphology observation, the powder was embedded in epoxy resin, and polished with the adequate recipe (presented in Annex A). The sample in Figure 3.5 was obtained and was observed recurring to a Zeiss optical microscope with an Infinity 2 digital camera, acquiring Figure 3.6. Analysing the photo, we can affirm that the powder has a spherical morphology, also ideal for L-PBF printing.

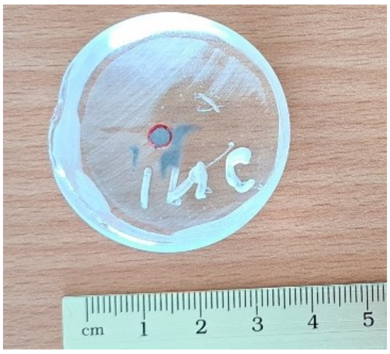

Figure 3.5 Inconel 625 powder embedded in polished Epoxy resin.

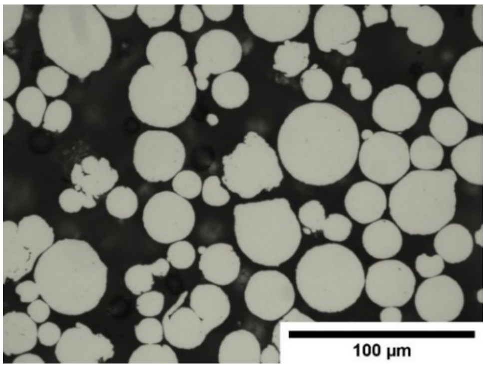

Figure 3.6 Cross-section of the Inconel 625 powder obtain with an optical microscope, to observe its morphology.

## 3.2 Ability to produce the geometry with L-PBF

The geometry selected to produce is complex. To certify that the mesh is printable using L-PBF, and to foresee possible hurdles, two meshes were printed using Ti-6Al-4V, since the powder was already available and had been previously inserted in L-PBF.

The .STL files and the designs were created using the software Autodesk Fusion 360, with the dimensions for Mesh #1 mentioned by Raminhos, J. et al. [1]. Two different meshes were designed with $\theta$ of 15$^{o}$ and "a" equal to "b" of 10mm. The width is equal to thickness, and is 1 mm or 0.5mm, as presented in Figure 3.7. 1mm was the value suggested for the base model in Raminhos, J. *et al* [1], and 0.5mm was selected to experiment and analyse the ability of L-PBF to print correctly a mesh with smaller dimensions. There were also made the .STL files for other measurements of t as 2mm, and mesh #2 with a t of 0.5, 1 and 2 mm, whose dimensions are available at Annex C.

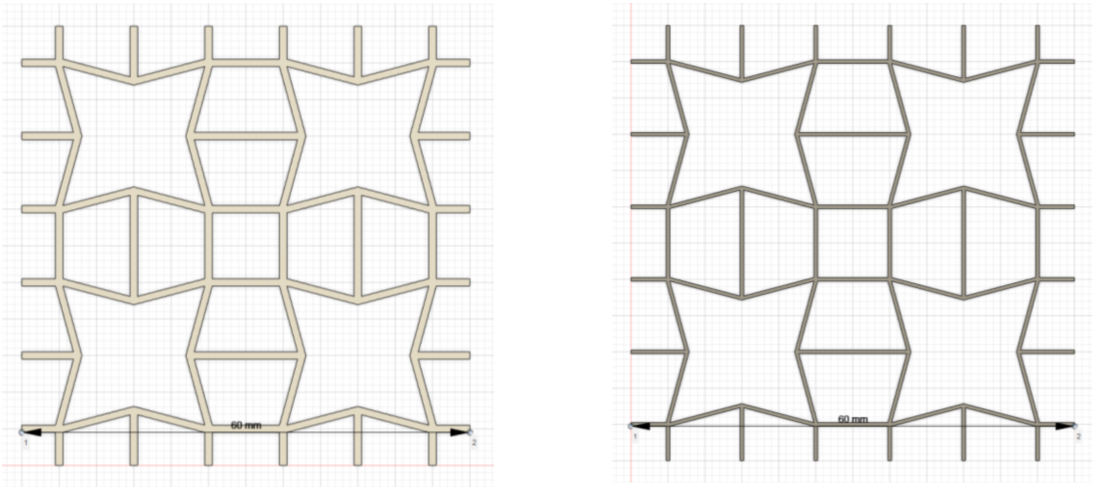

Figure 3.7 Designed meshes on Autodesk Fusion 360.

After printing, with the intent to separate the mesh from the supports, some methods were studied. Starting with the 1mm mesh, the supports were removed using a hand saw, as described in Annex A, but it had the disadvantage of being difficult to position and cut at first try, resulting in an uneven surface.

While separating the build plate from the supports, some warping was observed, therefore, the 0.5mm mesh was subjected to a heat treatment for one hour at 500$^{o}$C in an argon atmosphere and left to cool inside the oven. After treatment the supports were removed using a hand polisher and a screwdriver. During and after removal, the mesh did not warp as much as 1mm mesh, but that effect was still present, possibly due to the method of removing supports. The meshes printed are presented in Figure 3.8.

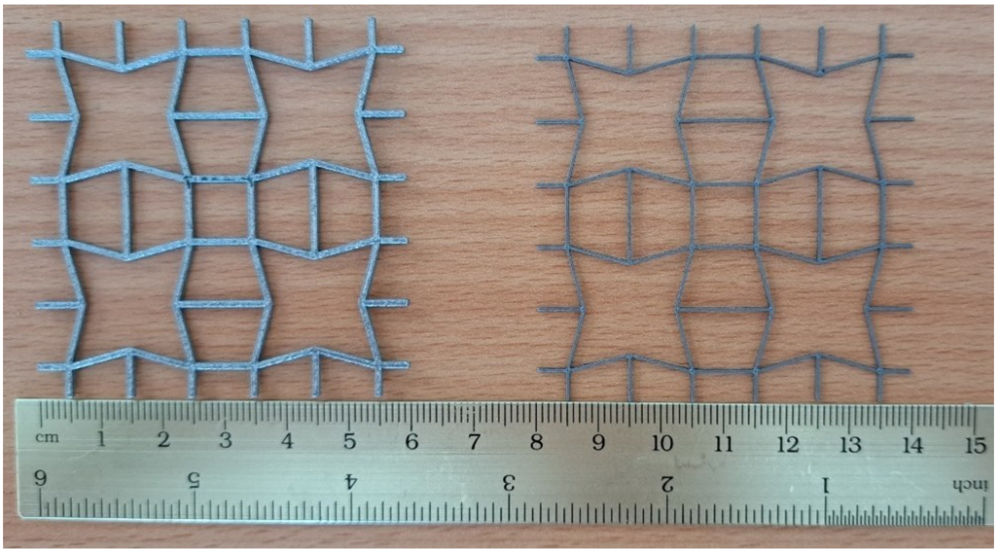

Figure 3.8 First meshes printed in L-PBF with the width of, respectively from left to right, 1.0mm and 0.5mm.

To evaluate the accuracy in the printing process, some measurements were taken from both meshes with a Vernier caliper, being presented in Table 3.1, and compared with their theoretical values. No measurements of the thickness, “t” was taken, as while separating the 1mm mesh from supports, the structure was not sawed straight, presenting regions where “t” was significantly smaller, making that measurement highly imprecise.

According to everything presented, we can infer that the equipment is able to produce the geometry correctly with both widths. The 0.5 mm mesh also allowed to verify that the reduced thickness allowed the mesh to be manually compressed and pulled easily.

Table 3.1 Measurements taken from the firsts meshes printed.

| | *1mm mesh [mm]* | | *0.5 mm mesh [mm]* | |
|---|---|---|---|---|
| | Real | Theoretical | Real | Theoretical |
| *A* | 50.93±0.02 | 51.00 | 50.41±0.02 | 50.50 |
| *B* | 9.08±0.02 | 9.00 | 9.59±0.02 | 9.50 |
| *B1* | 9.05±0.02 | 9.00 | 9.61±0.02 | 9.50 |
| *C* | 8.09±0.02 | 8.045 | 7.89±0.02 | 7.863 |

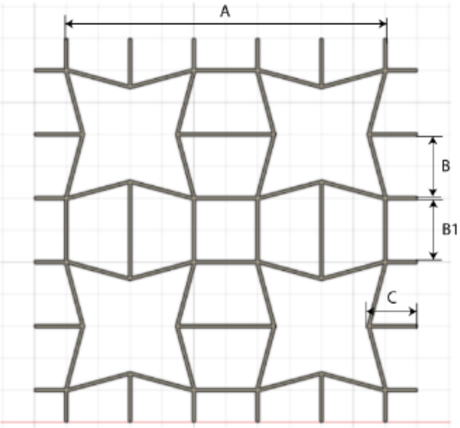

## 3.3 Parameters optimization

As previously seen, L-PBF is a complex technique of manufacturing, as the equipment presents a wide selection of parameters and options that can affect the final product. If the parameters are not adjusted for the material in use, several defects and problems whether internal or superficial, such as porosity, lack of fusion or as balling, and dimensional errors may surge [57].

To improve and correctly build the proposed structure, a parameter optimization needs to be performed. These parameters change due to several factors such as the material, the type of powders used, and the geometry of the piece. Thus, according to what has been exposed, a design of experiments, was carried out for each material used, specifically AlSi10Mg and Inconel 625. To make sure the studied parameters are not only tuned for the material but also for the geometry, the samples were printed with the unit cell design in Figure 1.2.

For AlSi10Mg as there was an ongoing work at ISQ from Salgueiro, F. master thesis, a typical DoE was not elaborated. Since a 3D object is nothing more than several single tracks together, layer by layer, making them the fundamental structural unit [35], in that work, single tracks with different parameters of the same material were printed. Using some of those parameters, for the present work, 18 samples were produced, and 7 different responses were measured. The responses studied were the average thickness (t), the deviation of the average thickness, the average width (w), the deviation of the average width, the average surface roughness (Ra), the porosity in the building direction and the porosity in the scanning direction.

Regarding the DoE for the IN625 alloy, out of the seven responses mentioned before, five were measured, excluding the deviations. The data analysis was made recurring to the Software Minitab. In Annex D, the processes and methods followed for the parameter optimization of both materials are described and justified in further detail.

The parameters that resulted in the best combination of responses, are presented in Table 3.2 for both materials studied. The 1st set of parameters for each material were the ones selected and used for the next steps of the present work.

Table 3.2 Top 3 results from the parameters optimization for AlSi10Mg and Inconel 625.

| | | *Sample* | *Power[W]* | *Velocity [mm/s]* | *Hatching distance [µm]* | *Layer thickness [µm]* |
|---|---|---|---|---|---|---|
| *AlSi10Mg* | 1st | 7 | 350 | 2250 | 90 | 30 |
| | 2nd | 4 | 250 | 2000 | 90 | 30 |
| | 3rd | 5 | 250 | 2500 | 90 | 30 |
| *Inconel 625* | 1st | 18 | 200 | 1500 | 80 | 30 |
| | 2nd | 1 | 100 | 500 | 80 | 30 |
| | 3rd | 15 | 200 | 1000 | 100 | 30 |

## 3.4 Analysis of the geometry with each material

As presented in the sub-chapter 3.1, the ability to produce the geometry in L-PBF has been confirmed. However, it is necessary to study if geometry and manufacturing technology changes the property of the constitutional materials, and if it presents the desired behaviour. Thus, with optimized parameters obtained and presented in sub-chapter 3.3, samples of AlSi10Mg and Inconel 625 were produced.

Firstly, to mechanically test the mesh, their design had to be altered adding anchoring holes, as presented in Figure 3.9. These are 2mm holes allowing the passage of a thread of NiTi wire for tensile tests to be performed.

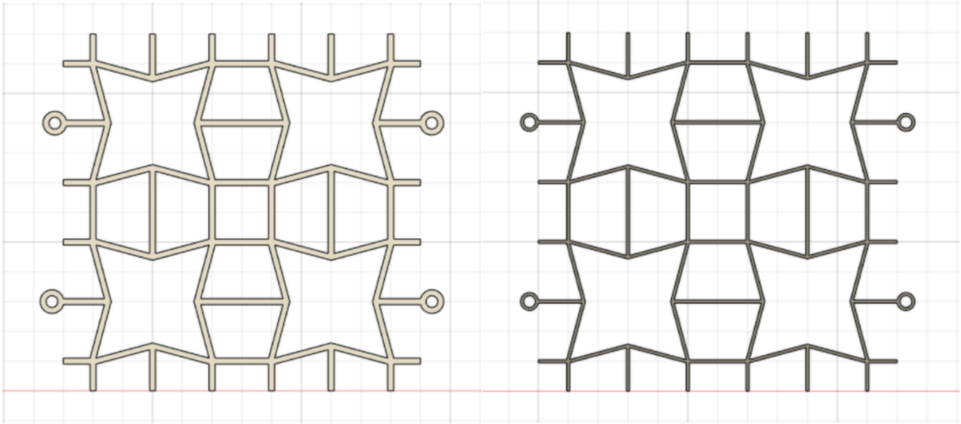

Figure 3.9 Designed meshes of 1mm and 0.5mm, respectively, with traction holes in Autodesk Fusion 360.

To continue the study of the meshes with 1mm and 0.5mm thickness, both were printed in each material with 3 replicas, totalling 12 samples. Every mesh was submitted to a heat treatment to reduce residual stress and avoid warping. IN625 samples were treated for 3 hours at 870°C and left to cool inside the furnace. AlSi10Mg meshes, were treated for 2 hours at 300°C, also left to cool inside. In the end, the meshes presented a slight warp.

The mechanical tests performed on the printed meshes were executed at NOVA University, recurring to a Shimadzu AG-50kNG universal testing. The meshes were evaluated at room temperature, through a tensile effort applied to induce a constant elongation rate of 1 mm/s until fracture. Every test was videorecorded, and the data was saved to elaborate the Strain vs Stress curves for each test, as presented in Figure 3.10 for 1mm and in Figure 3.11 for 0.5mm.

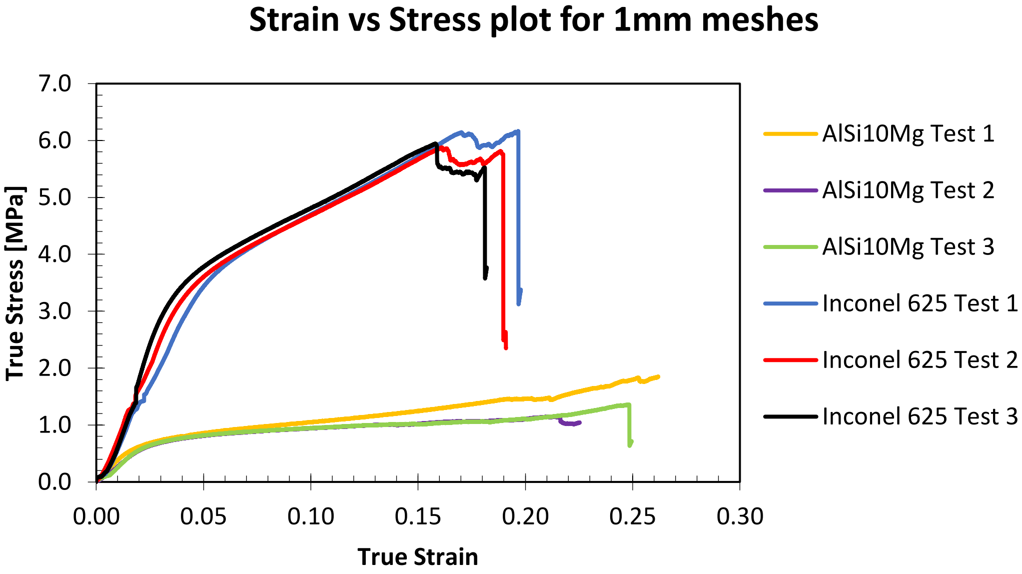

Figure 3.10 Strain vs stress for AlSi10Mg and INC625 meshes with a thickness of 1mm.

For 1mm IN625 samples, a machine adjustment confirmed in video caused an artifact in the form of a step at around 1,5MPa; this had to be removed from the data shown, resulting in the discontinuity at that point. At the yield point, the struts connected to the anchor points for the tensile test straighten, as presented in Figure 3.12. When the strain reached 15% the meshes started to present cracks, with failure occurring around 17% strain.

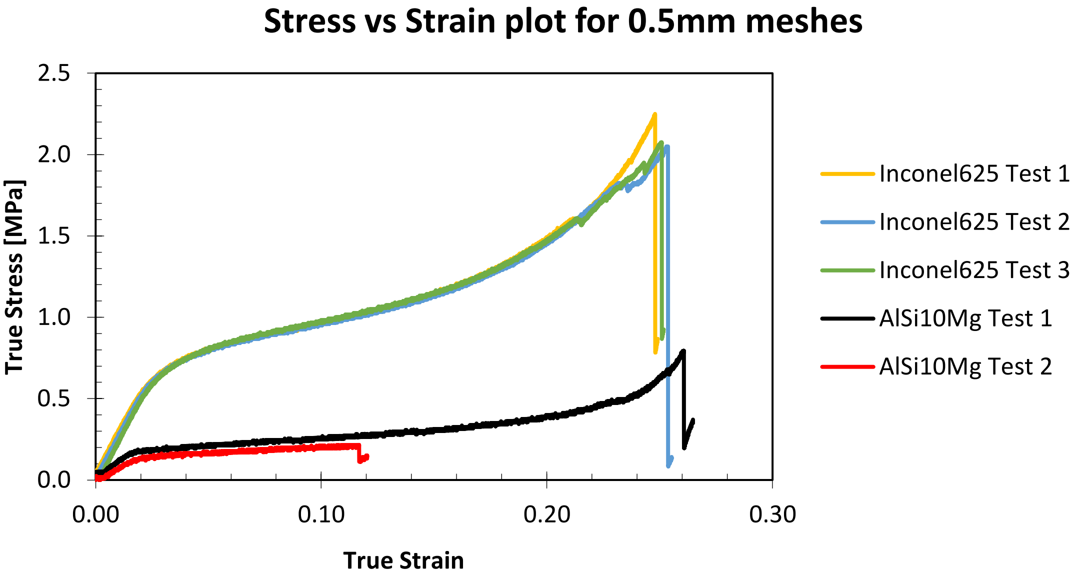

Figure 3.11 Strain vs stress curves for AlSi10Mg and IN625 Meshes with a thickness of 0.5mm.

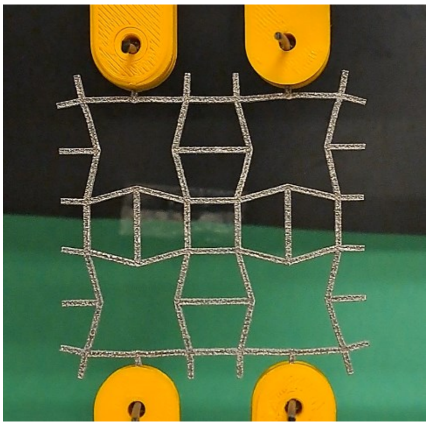

Figure 3.12 Example of the straightening of the struts connected to the anchor points for the tensile test.

Regarding the 1mm AlSi10Mg samples, the first test had to be stopped at 5 minutes, due to problems with the video recording, that may have caused relaxation of the material, especially since it was near its yield point, hence, the mesh could not be tested until fracture. The second test also could not be tested until fracture. These samples started to present fractures when the strain reached 21%. As predicted, for both materials was observed that the fractures occurred in connection points of the strut.

In IN625 meshes with 0.5mm, we can observe that the samples are ductile, presenting in the end a behaviour similar to elastic but when reaching a strain of 22,5% it starts to present cracks, ending in a fracture at around 25% strain.

There were 3 replicas of 0.5mm AlSi10Mg samples. When removing the supports from the structures, one broke not being subjected to a tensile test. As shown in Figure 3.11, Test 2 does not present a strain until fracture as high as test 1. Since the difference is high, the process of removing supports may cause cracking, which might had had an influence on the results. However, the behaviour was coincident but due to lack of replicas is not possible to analyse further.

Comparing both graphs, we can see the influence of the mesh thickness in the stress supported. IN625 with 1mm presented around 5% smaller strain than the 0.5mm mesh. AlSi10Mg presented the approximately same limit in strain for both values of t. In both graphs, it is possible to infer that the data are replicable.

To gain a clearer perspective of the meshes' resistance to deformation, the elastic modulus for each plot was measured. The average for each is presented in Table 3.3.

Table 3.3 Modulus of elasticity for the meshes mechanically tested.

| | | *Average [MPa]* | *Standard Deviation [MPa]* |
|---|---|---|---|
| *AlSi10Mg* | 1mm | 33.764 | ±3.634 |
| | 0.5mm | 9.090 | ±1.034 |
| *Inconel 625* | 1mm | 94.250 | ±20.114 |
| | 0.5mm | 25.640 | ±0.562 |

Considering the data gathered in Table 3.3, we can see that for the same thickness, whether 1mm or 0.5mm, Inconel presented a modulus of elasticity 2.8 times higher than AlSi10Mg. This relation is approximately verified for the bulk material, as shown in Table 2.1, where the ratio between IN625 and AlSi10Mg is around 2.7. Regarding the standard deviation of the meshes with 1mm of IN625, since these measurements are from the elastic domain, the slope presents a discontinuity in the middle due to machine adjustments, leading to a higher deviation between tests.

During mechanical tests, auxeticity was verified, as overlapping a mesh with other mechanically tests, it was possible to see that the vertical dimension had increased, and the horizontal had approximately maintained its dimensions, as presented in Figure 3.13. Thus, it is possible to infer that the meshes exhibit a near-zero Poisson ratio.

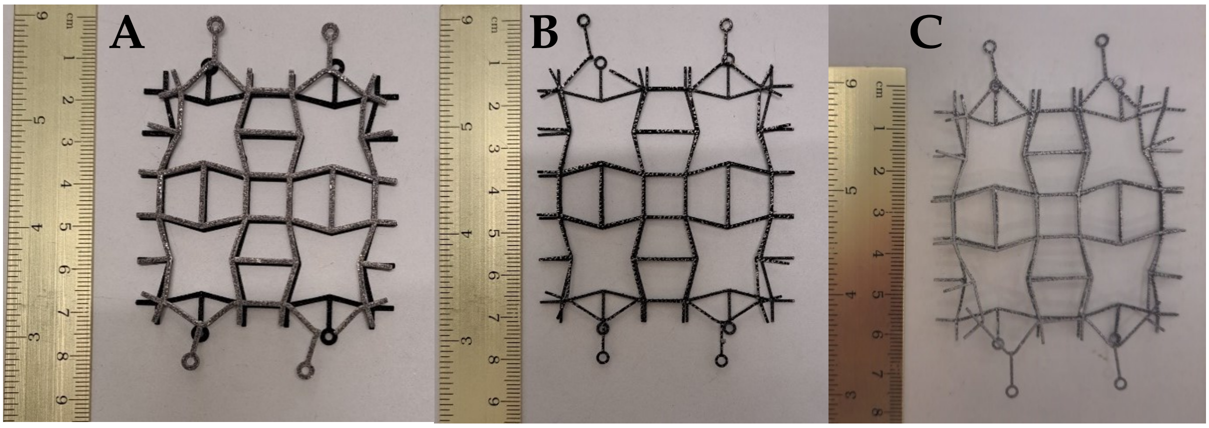

Figure 3.13 Overlapping of meshes in between tensile testing: A) AlSi10mg 1mm over INC625 1mm; B) INC625 0.5mm over its replica; C) AlSi10Mg 0.5mm over its replica.

Given that the mesh does not present a homogeneous structure, this means that during the test deformation does not occur in a uniform way, presenting a deformation gradient. This behaviour cannot be characterized by a single value of Poisson Ratio, but by a variation of it with the deformation that is obtained in the mesh.

With the objective to calculate the Poisson Ratio evolution, for each video, the interval of the elastic domain used to obtain the modulus of elasticity was temporally identified, where within every five seconds a photograph was taken. To correctly measure samples' nominal strain, recurring to the software ImageJ, eight measurements were attained from each image, as presented in Figure 3.14.

During data acquisition, once measuring points were not marked on the samples, the limits of the mesh were extremely hard to identify, as well as sometimes the mesh blended with the background due to lack of contrast. Combined with the uncertainty of placement the extreme points in each measurement, this method presented a high error and uncertainty, therefore the data exhibited a great fluctuation of values. Another problem identified is that when one of the directions presented a minimal variation, the Poisson ratio value at that point reached absurd levels, such as 40 or -30. Thus, the mathematical formulation of the Poisson ratio also incurred into difficulties.

Given that the data taken had coefficients with absurd values, and that between replicas the data cannot be compared at each instant or for the same values of strain. This is because the instant at which a sample begins its elastic domain is different from the others and the strain it presents will also vary because it cannot be guaranteed that they were under the same initial conditions.

On some occasions, in the tension direction, negative strain values raised. This is because as the structure is tensioned, the connection point marked with a yellow circle in Figure 3.14 used for measuring, undergoes a rotation around the tensile axis resulting in a decrease in strain even though at middle points, marked by a green circle, in each unit cell the strain increases with the given 1mm per second. This can be observed in Figure 3.13 C where the top left corner is lower than the base model.

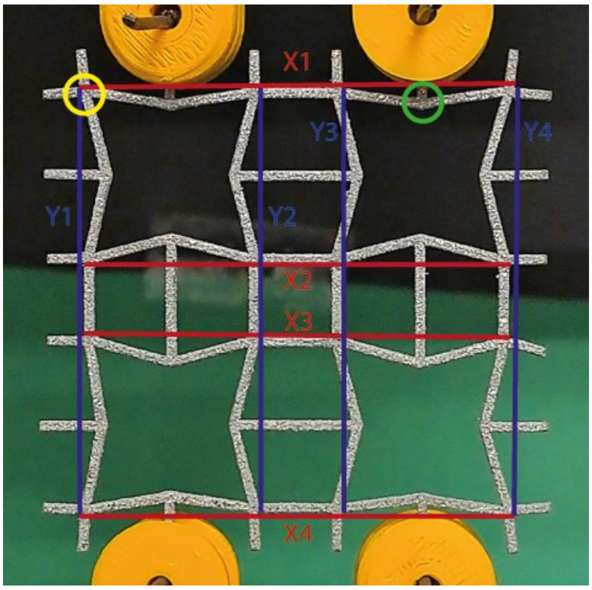

Figure 3.14 Mesh at the start of tensile test, with the identification of measurements taken.

## 3.5 Bimetallic Meshes

To achieve the anepectic behaviour, it is necessary that the equipment be capable of printing two different materials simultaneously. Since the equipment available can only print one material at a time, some strategies were thought to successfully build bimetallic meshes. However, the strategies were extremely hard to accomplish, due to a high precision to deposit and spread thin layers of powder manually or due to the equipment's own working principle.

To prepare designs to print with two materials, two more had to be made. One is the structure without the second material connective beams, as presented in Figure 3.15 A and the other is only the connective beams, meant to be with the second material.

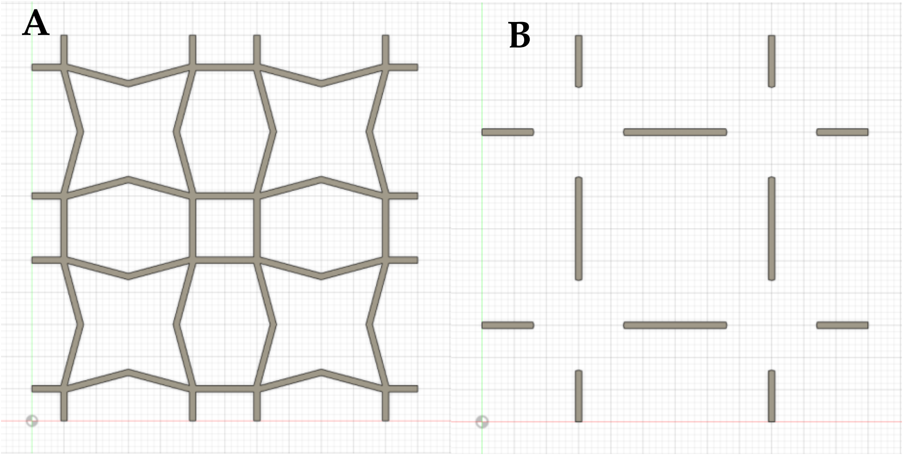

Figure 3.15 Design to print with two materials. A) Structure without beams; B) Only the structural beams.

One strategy was to print the mesh without the beams of AlSi10Mg (Figure 3.15 A) and when printing the last 0.2µm for 1mm mesh or the last 0.1µm for 0.5mm, the printing would stop. The inputted design would change to a complete mesh, and then print the rest with the same material. When it reached the final dimension, the printing would stop and the design with only the beams (Figure 3.15 B) would be inputted and the material changed, continuing the printing process for a height of around 0.3µm, so that the intended structure would be possible to achieve. Due to lack of time, this was not tested, since first the interaction between the two materials had to be studied.

As a last option, one way to build the structure may be to print the first mesh in Inconel625 and, separately, print the AlSi10Mg beams. After production, both would be united by brazing. Both parts were printed, but there was not time to unite both parts.

## AlSi10Mg/Inconel625

It was printed a unit cell of AlSi10Mg, and the same structure in IN625 was printed directly printed on top of it, to study the interaction between the two materials. Two cells were printed, one with 1mm and other with 0.5mm, as presented in Figure 3.16 A. As observed in Figure 3.16 A and B, there was a lack of adhesion between the materials in both cells, however the cell with 0.5 mm presented better adhesion, although it also presented cracks at the interface between the two materials.

To understand the materials' interfacing issues, parts of both cells were cold-mounted in epoxy resin to analyse under scanning electron microscopy (SEM). In Figure 3.16 C is the embedded bimetallic meshes, specifically a 0.5mm in the building direction, 1mm in building direction and scanning direction, and another sample produced AlSi10Mg/Inconel/AlSi10Mg.

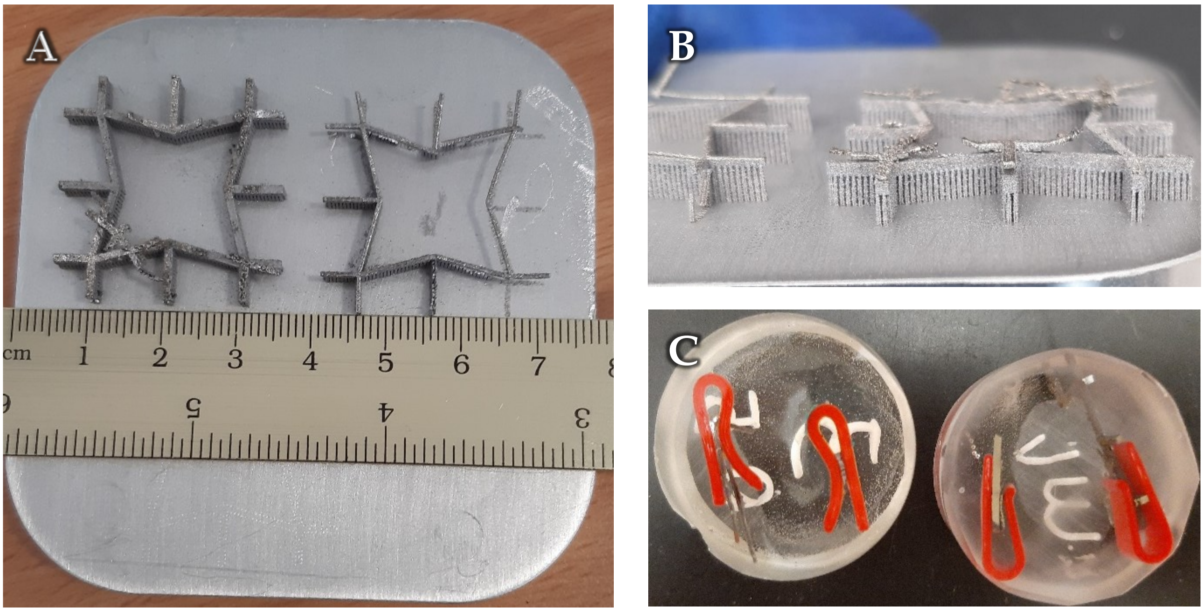

Figure 3.16 Unit cells bimetallic. A) presents the build plate after printing. B) the Scanning direction of the 1mm cell. C) parts of the unit cells putted together by a clamp, embedded in polished epoxy resin.

For the analysis of AlSi10Mg/Inconel625 cells, a Zeiss DSM 962 microscope, available in CENIMAT at NOVA SST was used (presented in Annex A). Recurring to an elemental analysis, in Figure 3.17 we see the 0.5mm cell in building direction, with a line crossing the interface between materials where we have the distribution of elements in the sample. The dark grey represents AlSi10Mg and the light grey Inconel 625. The dark spots in the AlSi10Mg interface are agglomerations of Si, Al and Oxygen, since the fabrication process is in an Argon atmosphere, we may infer that the Oxygen present comes from the material and it is clustered in that area.

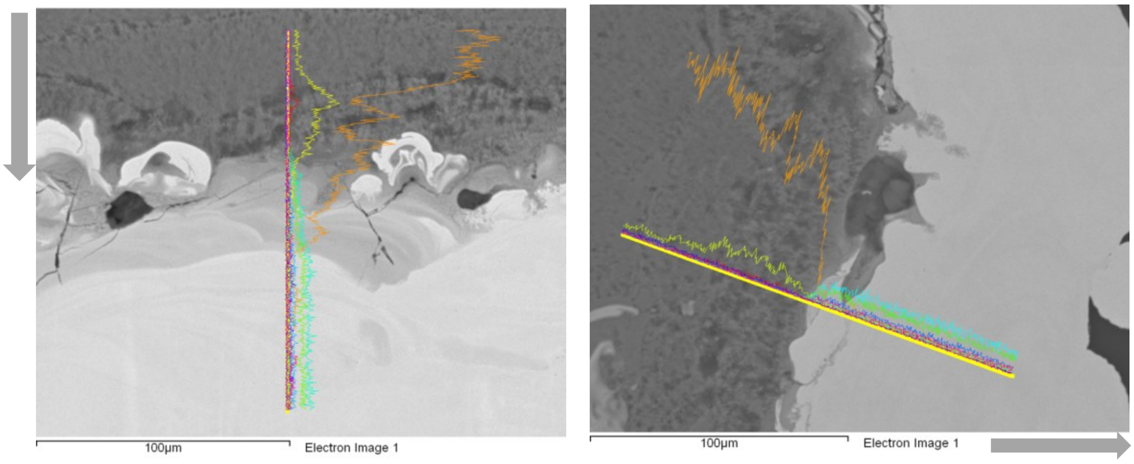

Figure 3.17 AlSi10Mg/IN625 SEM images with elemental analysis. The orange line represents Al, the yellow Si, green is Cr and in turquoise is Ni. The arrows indicate the building direction.

As observed in Figure 3.17, there are cracks in the AlSi10Mg/IN625 interface area, which may be attributed to precipitation of fragile intermetallic compounds, making the interface the interface weak and prone to cracking. This side effect was observed in every sample observed. There are visible some pores in the interface, that may be caused due to the difference between both powder's size.

Since AlSi10Mg was firstly printed, the patterns drawn by these dark spots consist of distinct and partially overlapped melt pools, as confirmed with some literature [58]–[60]. These are noticeable in some observations, such as the ones obtained with OM, presented in Figure 3.18.

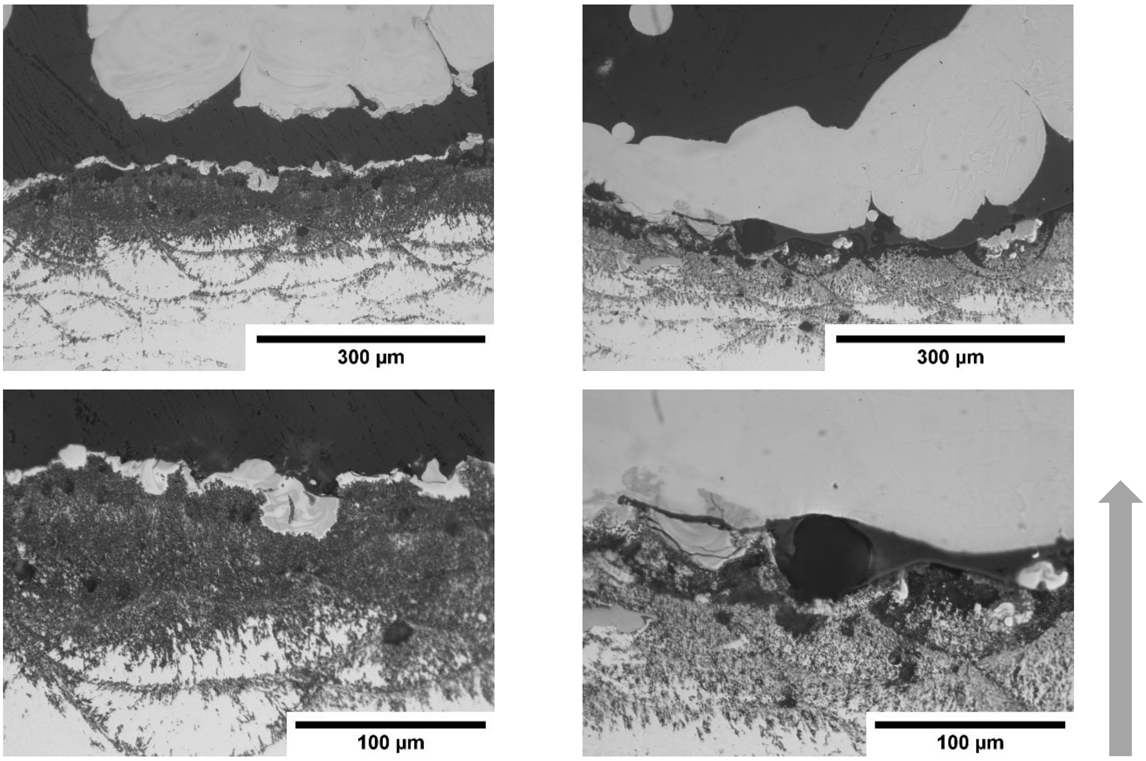

Figure 3.18 Optical microscopy images of bimetallic samples, where it is observable the melt pools in AlSi10Mg side. The arrow represents the building direction.

## AlSi10Mg/Inconel 625/AlSi10Mg

A 3-layer beam was printed, to experiment other ways to build the connective beams presented in Figure 3.15 B. The deposition started with AlSi10Mg, then IN625 and AlSi10Mg again, each layer with a theoretical 0.3µm height and 0.5µm width.

In the images taken from both microscopies it is possible to see the mixture between the materials. It was programmed 0.3µm layers for each material.

In Figure 3.19 it is possible to observe the elemental analysis made of the 3-layered sample. The first and second materials deposited, contrary to what was verified in the last sub-chapter, they were well mixed this time with some visible interdiffusion, as evidenced by an intermediate shade of grey. The fact that they mix with each other is a good outcome, as a small area of interdiffusion is desired and they can be worked recurring to a parameter optimization to improve their compatibility. AlSi10Mg has a smaller fusion point than IN625, thus when melting a material with a higher melting point over one with lower, it is easier for them to mix.

In the second part of the sample, the interface between materials is now clearly defined, since the temperature is not enough to melt and mix the two layers. This factor is not ideal since the clearer the separation between materials, easier it is to nucleate cracks at the interface. When comparing this sample with the bimetallic AlSi10Mg/IN625, we see that the cracking was not as intense, but still existent, mostly as microfractures.

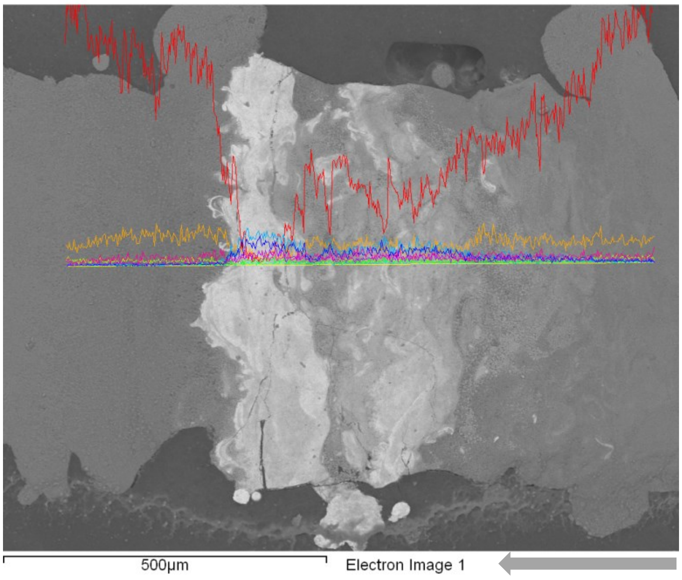

Figure 3.19 AlSi10Mg/IN625/AlSi10Mg SEM image with an elemental analysis. In red its represented Aluminium, in orange its Silicon, in dark blue is Chromium and in light blue is Nickel. The arrow represents the building direction

## Inconel 625/AlSi10Mg

To further analyze the compatibility of both materials, a mesh with AlSi10Mg over Inconel 625 was printed. Considering the same support removal technique, this mesh presented the best cohesion between materials, as little separation was observed according to Figure 3.20 A. Similarity to other samples, small pieces were embedded and observed in a SEM. The specimen was observed with an optical microscope and with the SEM XMAX JEOL JSM 6500F available at ISQ (presented in Annex A).

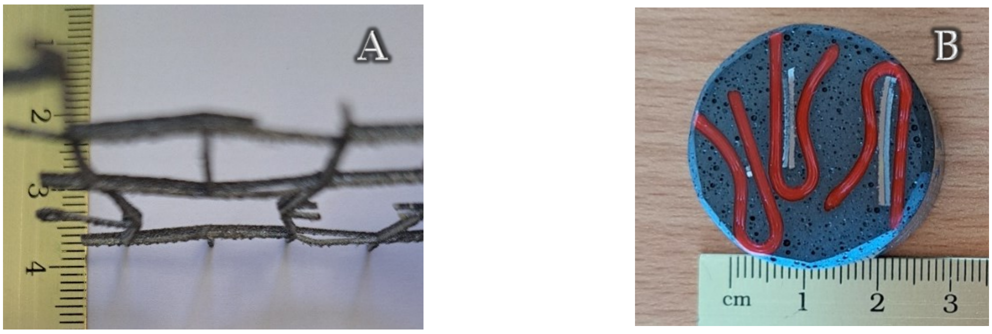

Figure 3.20 IN625/AlSi10Mg mesh. A) Side view of the produced mesh after parts extraction for observation. B) Embedded parts for observation.

When observing the sample using optical microscopy in Figure 3.21, it was possible to identify a small area with the third coloration, as seen in the previous sections. This was as expected, since in the 3-layered sample the interface between IN625 and AlSi10Mg was clearly identified, and little mixture was verified. However, in the other two samples observed in SEM, both barely presented the third coloration in the specimen, as observed in Figure 3.21 C. A SEM analysis was performed and both materials components are identified, allowing us to infer that interdiffusion also occurs. Since the fracture appears mainly in this area, it is possible to conclude that the compounds created are fragile. In the other two samples embedded, cracks were also identified in the interface as well as lack of fusion.

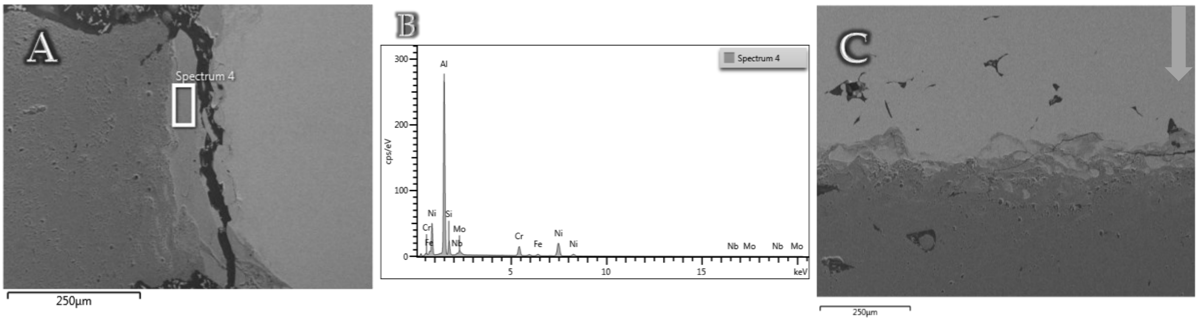

Figure 3.21 A) SEM analysis of the interface between materials, with elements distribution available in B). C) Image of the interface observed with SEM.

To better understand the patterns and algomerations formed, te samples were etched with a Kellers'reagent. For a clearer idea of the changes attainded in the specimen, we can see Figure 3.22, where a before etching Figure (A) and after etching (B) are presented. In the images, it can be noticed the region where there was a mixture between the materials, where the Al-rich region appear bright and the Ni-rich is dark. Comparing the before and after etching, we can see the grains are more visible.

In Figure 3.22 B and C its identifiable that melt pools boundaries present bigger cells with a dendritic shape, directed toward pool centers from following thermal gradients during solidification and due to reheating caused by subsequent passes of the laser and the changes in the solidification conditions, as confirmed with literature [59], [61].

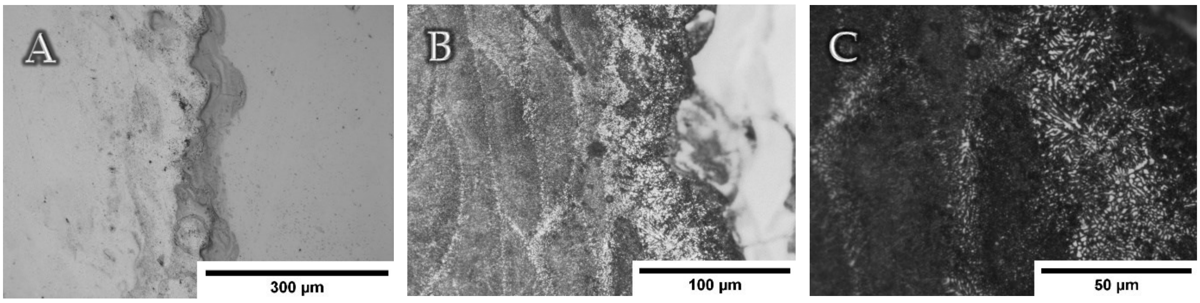

Figure 3.22 IN625/AlSi10Mg mesh observed under optical microscopy. A) Without contrast, with focus on the interface. B) Zoom on the AlSi10Mg part with contrast. B) AlSi10Mg part with contrast, with focus on melt pools patterns.

# 4

# CONCLUSIONS AND FUTURE PERSPECTIVES

Taking advantage of the additive manufacturing technology, a two-dimensional re-entrant star-shaped metal structure was successfully manufactured by laser-powder bed fusion. Striving to achieve anepectic behaviour, as it can only be observed when the two constituent materials presented similar but different stiffness values and widely different CTE, two materials were carefully selected, namely Inconel 625 and AlSi10Mg.

AM is a highly complex manufacturing technique, and to prevent high porosity, roughness, and dimensional errors, the parameters used for each material were optimized and three parameters' sets were attained for each material.

It was confirmed that the structure can be printed correctly with L-PBF, two meshes were successfully printed, and with good dimensional accuracy. However, some challenges were identified during support removal, with the appearance of warping sometimes promoted by the technique used. In addition, the cutting machine was not sufficiently precise to cut the supports completely or evenly.

As a way to establish a baseline for the behaviour of each material with the geometry, several meshes were produced and their mechanical behaviour was analysed. It could be observed that the metallic meshes presented auxetic behaviour, independently of the metallic alloy. The applied method to measure the Poisson' Ratio was not the most feasible and precise enough to detect small variations, which means that the used setup was not ideal to take the measurements needed. Therefore, it was difficult to obtain reliable data and more tests should be carried out to calculate the Poisson ratio.

To analyse the relationship and interconnection between the two selected materials, overlapping meshes were printed with the two alloys. This study allowed the observation of the interconnection between the two materials and the most prominent results were when IN625 was deposited first, with a small area of interdiffusion of the two materials.

In accordance with the recognised limitations of the manufacturing equipment, two strategies were devised. The first was to print the mesh without the connective structures and in the last layers of the printing process, change the design to the complete structure and, when reaching the designated thickness, add another 0.3cm of the connective structures. As a last option, one way to build the structure is to print the first mesh, in IN625 and separately, print the AlSi10Mg beams. After production, both would be joined by brazing. Both parts were printed, but due to time constraints, it was not possible to join both parts and the anepectic behaviour was not fully investigated, and a continuation of this study should be developed.

Regarding the further development of this thesis, it would be interesting to measure the thermal expansion coefficient of the single alloy meshes, as it is a crucial property for the anepetic behaviour. Due to the identification of an interdiffusion area, more studies must be also performed in order to clarify if intermetallic compounds are created, and a study of parameters for the combination of materials should be performed to optimize it, improving their bonding.

For future works, considering the work here presented, bimetallic meshes with adequately positioned materials must be manufactured to try to achieve anepectic behaviour and other material combinations should be tried out where the requirements for the behaviour are met.

# REFERENCES

[1] J. M. S. Raminhos, “Additive Fabrication of Anepectic Meshes.,” NOVA School of Science and Technology, 2018.

[2] J. Fan *et al.*, “A review of additive manufacturing of metamaterials and developing trends,” *Mater. Today*, vol. 50, no. November, pp. 303–328, 2021, doi: 10.1016/j.mattod.2021.04.019.

[3] J. S. Raminhos, J. P. Borges, and A. Velhinho, “Development of polymeric anepectic meshes: Auxetic metamaterials with negative thermal expansion,” *Smart Mater. Struct.*, vol. 28, no. 4, 2019, doi: 10.1088/1361-665X/ab034b.

[4] J. U. Surjadi *et al.*, “Mechanical Metamaterials and Their Engineering Applications,” *Adv. Eng. Mater.*, vol. 21, no. 3, pp. 1–37, 2019, doi: 10.1002/adem.201800864.

[5] T.-C. Lim, *Mechanics of Metamaterials with Negative Parameters*. Springer, 2020.

[6] A. A. Zadpoor, “Mechanical meta-materials,” *Mater. Horizons*, vol. 3, no. 5, pp. 371–381, 2016, doi: 10.1039/c6mh00065g.

[7] A. du Plessis *et al.*, “Properties and applications of additively manufactured metallic cellular materials: A review,” *Prog. Mater. Sci.*, vol. 125, no. April 2021, p. 43, 2022, doi: 10.1016/j.pmatsci.2021.100918.

[8] O. Abdulhameed, A. Al-Ahmari, W. Ameen, and S. H. Mian, “Additive manufacturing: Challenges, trends, and applications Manufacturing processes,” vol. 11, no. 2, pp. 1–27, 2019, doi: 10.1177/1687814018822880.

[9] E. Barchiesi, M. Spagnuolo, and L. Placidi, “Mechanical metamaterials: a state of the art,” *Math. Mech. Solids*, vol. 24, no. 1, pp. 212–234, 2018, doi: 10.1177/1081286517735695.

[10] G. N. Greaves, A. L. Greer, R. S. Lakes, and T. Rouxel, “Poisson’s ratio and modern materials,” *Nat. Mater.*, vol. 10, no. 11, pp. 823–837, Nov. 2011, doi: 10.1038/nmat3134.

[11] X. Ren, R. Das, P. Tran, T. D. Ngo, and Y. M. Xie, “Auxetic metamaterials and structures: a review,” *Smart Mater. Struct.*, vol. 27, no. 2, p. 023001, Feb. 2018, doi: 10.1088/1361-665X/aaa61c.

[12] J. Parada, “Additive Fabrication of electrically controlled Anepectic Meshes,” NOVA School of Science and Technology, 2019.

[13] Y. Liu and H. Hu, “A review on auxetic structures and polymeric materials,” *Science (80-. ).*, vol. 5, no. 10, pp. 1052–1063, 2010, [Online]. Available: http://www.academicjournals.org/SRE.

[14] W. E. I. Yang, Z. Li, W. E. I. Shi, B. Xie, and M. Yang, “Review on auxetic materials,” *J. Mater. Sci.*, vol. 39, pp. 3269–3279, 2004.

[15] R. Lakes, “Foam Structures with a Negative Poisson’s Ratio,” *Science (80-. ).*, vol. 235, no. 4792, pp. 1038–1040, Feb. 1987, doi: 10.1126/science.235.4792.1038.

[16] J. o. Cardoso, J. P. (CENIMAT/I3N. Borges, and A. (CENIMAT/I3N) Velhinho, “Structural metamaterials with negative mechanical/thermomechanical indices: A review,” *Prog. Nat. Sci. Mater. Int.*, p. 8, 2021, doi: 101.1016/j.pnsc.2021.10.015.

[17] F. Colmenero, “Revealing rutherfordine mineral as an auxetic material,” *Appl. Sci.*, vol. 8, no. 11, 2018, doi: 10.3390/app8112281.

[18] Y. Du, J. Maassen, W. Wu, Z. Luo, X. Xu, and P. D. Ye, “Auxetic Black Phosphorus: A 2D Material with Negative Poisson’s Ratio,” *Nano Lett.*, vol. 16, no. 10, pp. 6701–6708, 2016, doi: 10.1021/acs.nanolett.6b03607.

[19] F. Amin, M. N. Ali, U. Ansari, M. Mir, M. A. Minhas, and W. Shahid, “Auxetic Coronary Stent Endoprosthesis: Fabrication and Structural Analysis,” *J. Appl. Biomater. Funct. Mater.*, vol. 13, no. 2, pp. 127–135, Jul. 2015, doi: 10.5301/jabfm.5000213.

[20] Q. Liu, “Materials with Negative Poisson’s Ratios and Potential Applications to Aerospace and Defence,” Australia, 2006. [Online]. Available:

http://oai.dtic.mil/oai/oai?verb=getRecord&metadataPrefix=html&identifier=ADA460791.

[21] Y. Jiang *et al.*, “Auxetic Mechanical Metamaterials to Enhance Sensitivity of Stretchable Strain Sensors,” *Adv. Mater.*, vol. 30, no. 12, pp. 1–8, 2018, doi: 10.1002/adma.201706589.

[22] B. S. Mitchell, *An Introduction to Materials Engineering and Science*. 2003.

[23] K. (Nagoya U. Takenaka, “Negative thermal expansion materials: technological key for control of thermal expansion,” *Sci. Technol. Adv. Mater.*, vol. 13, no. 1, p. 013001, Feb. 2012, doi: 10.1088/1468-6996/13/1/013001.

[24] L. Wu, B. Li, and J. Zhou, “Isotropic Negative Thermal Expansion Metamaterials,” *Am. Chem. Soc. Appl. Mater. Interfaces*, 2016, doi: 10.1021/acsami.6b05717.

[25] W. Miller, C. W. Smith, D. S. MacKenzie, and K. E. Evans, “Negative thermal expansion: A review,” *J. Mater. Sci.*, vol. 44, no. 20, pp. 5441–5451, 2009, doi: 10.1007/s10853-009-3692-4.

[26] Z. Liu, Q. Gao, J. Chen, J. Deng, K. Lin, and X. Xing, “Negative thermal expansion in molecular materials,” *Chem. Commun.*, vol. 54, no. 41, pp. 5164–5176, 2018, doi: 10.1039/c8cc01153b.

[27] E. Liang, Q. Sun, H. Yuan, J. Wang, G. Zeng, and Q. Gao, “Negative thermal expansion: Mechanisms and materials,” *Front. Phys.*, vol. 16, no. 5, 2021, doi: 10.1007/s11467-021-1070-0.

[28] N. Shi, Y. Song, X. Xing, and J. Chen, “Negative thermal expansion in framework structure materials,” *Coord. Chem. Rev.*, vol. 449, pp. 1–52, 2021, doi: 10.1016/j.ccr.2021.214204.

[29] L. Ai and X. L. Gao, “Metamaterials with negative Poisson’s ratio and non-positive thermal expansion,” *Compos. Struct.*, vol. 162, pp. 70–84, 2017, doi: 10.1016/j.compstruct.2016.11.056.

[30] O. Sigmund and S. Torquato, “Composites with extremal thermal expansion coefficients,” vol. 69, no. November, pp. 3203–3205, 1996.

[31] X. Li, L. Gao, W. Zhou, Y. Wang, and Y. Lu, “Novel 2D metamaterials with negative Poisson ’ s ratio and negative thermal expansion,” *Extrem. Mech. Lett.*, vol. 30, pp. 1–9, 2019, doi: 10.1016/j.eml.2019.100498.

[32] N. Xu and H. T. Liu, “A novel 3-D structure with tunable Poisson’s ratio and adjustable thermal expansion,” *Compos. Commun.*, vol. 22, no. May, 2020, doi: 10.1016/j.coco.2020.100431.

[33] I. Marcelino, “Additive Fabrication of Anepectic Meshes controlled by a NiTi alloy,” NOVA School of Science and Technology, 2019.

[34] J. P. Oliveira, T. G. Santos, and R. M. Miranda, “Revisiting fundamental welding concepts to improve additive manufacturing: From theory to practice,” *Prog. Mater. Sci.*, vol. 107, no. June 2019, p. 100590, 2020, doi: 10.1016/j.pmatsci.2019.100590.

[35] S. A. Yadroitsev, Igor (Department of mechanical and mechatronic Engineering, Central University of Technology, Bloemfontein, Free State, S. A. Yadroitsava, Ina (Department of Mechanical and Mechatronic Engineering, Central University of Technology, Bloemfontein, Free State, N. M. du Plessis, Anton (Department of Mechanical Engineering, S. A. University, Port Elizabeth, Eastern Cape, South Africa; Research Group 3D Innovation, Stellenbosch University, Stellenbosch, Western Cape, and U. S. MacDonald, Eric (W. M. Keck Center for 3D Innovation, University of Texas at El Paso, El Paso, TX, *Fundamentals of Laser Powder Bed Fusion of Metals*. Elsevier.

[36] C. Wei and L. Li, “Recent progress and scientific challenges in multi- material additive manufacturing via laser-based powder bed fusion,” *Virtual Phys. Prototyp.*, vol. 16, no. 3, pp. 347–371, 2021, doi: 10.1080/17452759.2021.1928520.

[37] M. Binder *et al.*, “Potentials and Challenges of Multi-Material Processing by Laser-Based Powder Bed Fusion,” in *Solid Freeform Fabrication Symposium*, 2018, pp. 376–387, doi: http://dx.doi.org/10.26153/tsw/17025.

[38] W. E. King *et al.*, “Laser powder bed fusion additive manufacturing of metals; physics, computational, and materials challenges,” *Appl. Phys. Rev.*, vol. 2, no. 4, p. 041304, 2015, doi: 10.1063/1.4937809.

[39] S. Vock, B. Klöden, A. Kirchner, T. Weißgärber, and B. Kieback, “Powders for powder bed fusion:

a review," *Prog. Addit. Manuf.*, vol. 4, no. 4, pp. 383–397, Dec. 2019, doi: 10.1007/S40964-019-00078-6/TABLES/3.

[40] Renishaw, "RenAM 500Q / T / D / S additive manufacturing system," 2019, [Online]. Available: https://resources.renishaw.com/download.aspx?data=106560&lang=en&showForm=true&&RPSAction=Login&RPSUserXfer=de020c68-af61-420e-9420-da13c7af63ed.

[41] Renishaw, "In625-0402 powder for additive manufacturing," 2017. [Online]. Available: http://resources.renishaw.com/en/download/data-sheet-alsi10mg-0403-400-w-powder-for-additive-manufacturing--73122.

[42] Renishaw, "SS 316L-0407 powder for additive manufacturing * H-5800-3001-03-A *," vol. 2001, pp. 3–4, 2001.

[43] Renishaw, "AlSi10Mg-0403 powder for additive manufacturing * H-5800-1084-01-B *," vol. 2001, no. Iso 97, pp. 1–3, 2001, [Online]. Available: http://resources.renishaw.com/en/download/data-sheet-alsi10mg-0403-400-w-powder-for-additive-manufacturing--73122.

[44] E. L. Rooy and J. H. L. Van Linden, "ASM Metals Handbook, Properties and Selection: Nonferrous Alloys and Special-Purpose Materials," vol. 2, pp. 3330–3345, 1990.

[45] "Aluminum 2319." https://www.matweb.com/search/DataSheet.aspx?MatGUID=0cd9a7263d7f45879dfd1d60b8e312e6 (accessed Aug. 09, 2022).

[46] "2319 Aluminum Alloy Plate | WixSteel Industrial." https://www.wixsteel.com/products/aluminum-alloy/2000-series-aluminum-alloy/2319 (accessed Aug. 09, 2022).

[47] J. Zhou, X. Han, H. Li, S. Liu, and J. Yi, "Investigation of layer-by-layer laser remelting to improve surface quality, microstructure, and mechanical properties of laser powder bed fused AlSi10Mg alloy," *Mater. Des.*, vol. 210, p. 110092, Nov. 2021, doi: 10.1016/J.MATDES.2021.110092.

[48] C. A. Terrazas-Najera *et al.*, "Effects of process interruptions on microstructure and mechanical properties of three face centered cubic alloys processed by laser powder bed fusion," *J. Manuf. Process.*, vol. 66, pp. 397–406, Jun. 2021, doi: 10.1016/J.JMAPRO.2021.04.013.

[49] A. Majeed, A. Ahmed, A. Salam, and M. Z. Sheikh, "Surface quality improvement by parameters analysis, optimization and heat treatment of AlSi10Mg parts manufactured by SLM additive manufacturing," *Int. J. Light. Mater. Manuf.*, vol. 2, no. 4, pp. 288–295, Dec. 2019, doi: 10.1016/J.IJLMM.2019.08.001.

[50] L. Wang, X. Jiang, M. Guo, X. Zhu, and B. Yan, "Characterisation of structural properties for AlSi10Mg alloys fabricated by selective laser melting," *https://doi.org/10.1080/02670836.2017.1398513*, vol. 33, no. 18, pp. 2274–2282, Dec. 2017, doi: 10.1080/02670836.2017.1398513.

[51] F. Zhang *et al.*, "Effect of heat treatment on the microstructural evolution of a nickel-based superalloy additive-manufactured by laser powder bed fusion," *Acta Mater.*, vol. 152, no. March 2019, pp. 200–214, 2018, doi: 10.1016/j.actamat.2018.03.017.

[52] Z. Tian *et al.*, "A review on laser powder bed fusion of Inconel 625 nickel-based alloy," *Appl. Sci.*, vol. 10, no. 1, 2020, doi: 10.3390/app10010081.

[53] Renishaw, "Reduced Build Volume for AM systems," vol. i, 2019, [Online]. Available: https://www.renishaw.com/resourcecentre/en/details/(d300f2b4-3a5c-480b-9339-04c274ff629b).

[54] Renishaw Plc., "QuantAM file preparation software for Renishaw additive manufacturing systems QuantAM – quick to learn , intuitive to use," 2015, [Online]. Available: https://www.renishaw.com/en/quantam-build-preparation-software--35455.

[55] G. A. Lujan-Moreno, P. R. Howard, O. G. Rojas, and D. C. Montgomery, "Design of experiments and response surface methodology to tune machine learning hyperparameters, with a random forest case-study," *Expert Syst. Appl.*, vol. 109, pp. 195–205, Nov. 2018, doi:

10.1016/J.ESWA.2018.05.024.

[56] D. C. A. S. U. Montgomery, *Design and Analysis of Experiments*, 9th ed. 2017.

[57] N. Sanaei and A. Fatemi, “Defect-based fatigue life prediction of L-PBF additive manufactured metals,” *Eng. Fract. Mech.*, vol. 244, no. January, p. 107541, 2021, doi: 10.1016/j.engfracmech.2021.107541.

[58] H. Qin, V. Fallah, Q. Dong, M. Brochu, M. R. Daymond, and M. Gallerneault, “Solidification pattern, microstructure and texture development in Laser Powder Bed Fusion (LPBF) of Al10SiMg alloy,” *Mater. Charact.*, vol. 145, no. August, pp. 29–38, 2018, doi: 10.1016/j.matchar.2018.08.025.

[59] M. H. Nasab, D. Gastaldi, N. F. Lecis, and M. Vedani, “On morphological surface features of the parts printed by selective laser melting (SLM),” *Addit. Manuf.*, vol. 24, no. October, pp. 373–377, 2018, doi: 10.1016/j.addma.2018.10.011.

[60] J. Zhang, B. Song, Q. Wei, D. Bourell, and Y. Shi, “A review of selective laser melting of aluminum alloys: Processing, microstructure, property and developing trends,” *J. Mater. Sci. Technol.*, vol. 35, no. 2, pp. 270–284, 2019, doi: 10.1016/j.jmst.2018.09.004.

[61] M. H. Nasab, A. Giussani, D. Gastaldi, V. Tirelli, and M. Vedani, “Effect of surface and subsurface defects on fatigue behavior of AlSi10Mg alloy processed by laser powder bed fusion (L-PBF),” *Metals (Basel).*, vol. 9, no. 10, pp. 7–10, 2019, doi: 10.3390/met9101063.

[62] E. Bassoli, A. Sola, M. Celesti, S. Calcagnile, and C. Cavallini, “Development of laser-based powder bed fusion process parameters and scanning strategy for new metal alloy grades: A holistic method formulation,” *Materials (Basel).*, vol. 11, no. 12, 2018, doi: 10.3390/ma11122356.

# A

# Equipments

## A.1 Struers Labotom-5 hand saw

The handsaw was used to separate the samples from the build plates. It consists of a cutting disc that rotates, cutting the metal where desired. This equipment comes with a cooling system, activated whenever the equipment starts working. The main challenge is to align the area where it is desired to be cut with the disc itself. In the present work, it was used few times, mainly to cut Ti-6Al-4V and the 0.5mm meshes for tensile tests.

Figure A.1 Struers Labotom-5 available at ISQ.

## A.2 EcoMet 30

EcoMet 30 from BUEHLER allows the manual polishing and grinding of samples. It consists of a base rotating counterclockwise with the speed selected with a knob switch. The equipment comes with 2 different bases, one mostly for grinding, where it is simple to change discs, and a magnetic base, ideal for polishing.

To prepare the samples of Inconel and AlSi10Mg, specific recipes were followed as presented in Table A.1 and Table A.2, respectively.

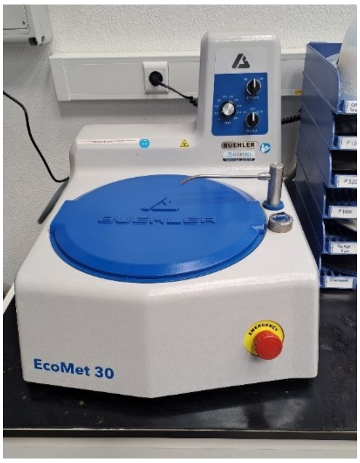

Figure A.2 EcoMet30 equipment available at ISQ.

Table A.1 Recipe followed for AlSi10Mg samples in EcoMet30 from BUEHLER

| Surface | Abrasive / Size | Load - lbs [N] / Specimen | Base Speed [rpm] | Relative Rotation | Time [min:sec] |
|---|---|---|---|---|---|
| Sectioning | Abrasive Cutter with a wheel recommended for use on non -ferrous materials | | | | |
| Mounting | Compression or Castable, typically with PhenoCure, EpoxiCure 2, EpoThin 2, or SamplKwick | | | | |
| CarbiMet | 320 [P400] grit SiC water cooled | 5 [22] | 300 | ● ⊛ | Until Plane |
| UltraPad | 9 µm MetaDi Supreme Diamond | 5 [22] | 150 | ● ⊛ | 5:00 |
| TriDent | 3 µm MetaDi Supreme Diamond | 5 [22] | 150 | ● ⊛ | 4:00 |
| TriDent | 1 µm MetaDi Supreme Diamond | 5 [22] | 150 | ● ⊛ | 2:00 |
| ChemoMet | 0.06 µm MasterMet Colloidal Silica | 5 [22] | 150 | ● ⊛ | 1:30 |

Table A.2 Recipe followed for Nickel samples in EcoMet30 from BUEHLER.

| Surface | Abrasive / Size | Load - lbs [N] / Specimen | Base Speed [rpm] | Relative Rotation | Time [min:sec] |
|---|---|---|---|---|---|
| Sectioning | Abrasive Cutter with a wheel recommended for use on SuperAlloys | | | | |
| Mounting | Compression, typically with EpoMet | | | | |
| CarbiMet | 240 [P280] grit SiC water cooled | 6 [27] | 300 | ● ⊛ | Until Plane |
| UltraPad | 9 µm MetaDi Supreme Diamond | 6 [27] | 150 | ● ⊛ | 5:00 |
| TriDent | 3 µm MetaDi Supreme Diamond | 6 [27] | 150 | ● ⊛ | 3:00 |
| TriDent | 1 µm MetaDi Supreme Diamond | 6 [27] | 150 | ● ⊛ | 2:00 |
| ChemoMet | 0.02 -0.06 µm MasterMet or MasterMet 2 Colloidal Silica | 6 [27] | 150 | ● ⊛ | 2:00 |

## A.3 Powder Sieve

The equipment used was from CISA, more specificallyIn the top sieve that has a wider mesh, the powder is deposited. The powders are sieved recurring to a vibrational movement of the sieves, and for the present work, the powders were shaked for 15 minutes.

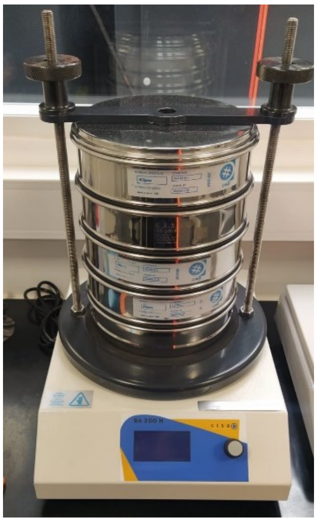

Figure A.3 CISA BA200N

## A.4 Furnace

For the thermal treatment of the meshes, a Nabertherm furnace was used. The equipment is presented in the figure below.

Figure A.4 Nabertherm furnace used.

## A.5 Optical microscopy

For observation of the embedded samples, optical microscopy was used. Connected to the microscope is the computer used for observation.

Figure A.5 Axiotech microscope with a Zeiss infinity 2 digital camera.

## A.6 Scanning electron microscopy

Two different SEMs were used to observe the embedded samples. Both are presented below.

Figure A.6 Scanning electron microscopies used. A) Zeiss DSM 962 at NOVA (Source: CENIMAT website); B)JEOL, JBM-B500F at ISQ facilities.

# B

# Powder characterization

## B.1 AlSi10Mg

The initial mass of powder measured was 203.560g. With that, the following weights were registered, and with that the powder size distribution was achieved.

Table B.1. Data acquired for the granulometric analysis performed on AlSi10Mg.

| ***[um]*** | ***Individual mass [g]*** | ***Cumulative mass [g]*** | ***Particles passed through [%]*** | ***Particles contained [%]*** |
|---|---|---|---|---|
| *63* | 73.455 | 73.455 | 36.085 | 36.085 |
| *45* | 109.122 | 182.577 | 53.607 | 89.692 |
| *38* | 18.583 | 201.160 | 9.129 | 98.821 |
| *2* | 0.100 | 201.260 | 0.049 | 98.870 |
| *<2* | 0.000 | 201.260 | 0.000 | 98.870 |
| *Total* | 201.260 | | 98.870 | |

Table B.2. Weight percentage according to the AlSi10Mg powders' size.

| | ***Weight content [%]*** | ***Cumulative weight [%]*** |
|---|---|---|
| *<20* | 0.000 | 0.000 |
| *20-38* | 0.049 | 0.049 |
| *38-45* | 9.129 | 9.178 |
| *45-63* | 53.607 | 62.785 |
| *>63* | 36.085 | 98.870 |

## B.2 Inconel 625

The initial mass of powder measured was 270.497g. With that, the following weights were registered, and with that the powder size distribution was achieved.

Table B.3. Data acquired for the granulometric analysis performed on IN625.

| ***[mm]*** | ***Individual mass [g]*** | ***Cumulative mass [g]*** | ***Particles passed through [%]*** | ***Particles contained [%]*** |
|---|---|---|---|---|
| *0.063* | 7.354 | 7.354 | 2.719 | 2.719 |
| *0.045* | 212.032 | 219.386 | 78.386 | 81.105 |
| *0.038* | 13.437 | 232.823 | 4.968 | 86.072 |
| *0.02* | 30.468 | 263.291 | 11.264 | 97.336 |
| *<0,02* | 3.489 | 266.780 | 1.290 | 98.626 |
| *Total* | 266.780 | | 98.626 | |

Table B.3 Weight percentage according to the IN625 powders' size.

| | ***Weight content [%]*** | ***Cumulative weight [%]*** |
|---|---|---|
| *<20* | 1.290 | 1.290 |
| *20-38* | 11.264 | 12.554 |
| *38-45* | 4.968 | 17.521 |
| *45-63* | 78.386 | 95.907 |
| *>63* | 2.719 | 98.626 |

# C

# Unit cells dimentions

For the meshes designs, it was considered that the unit cell is 30mm x 30mm. Three different meshes were designed, more specifically with t varying from 0.5mm to 1mm and 2mm. Despite the variations present in Raminhos, J. masters' thesis, it was only considered the mesh#1, where Θ= 15°. In the following schematics, the dimensions for the 1mm and 2mm meshes are presented.

Considering a unit cell, for a t of 1mm, the ¼ of the mesh has the dimensions presented in Figure C.7 and for the 2mm mesh, the dimensions are presented in Figure C.8.

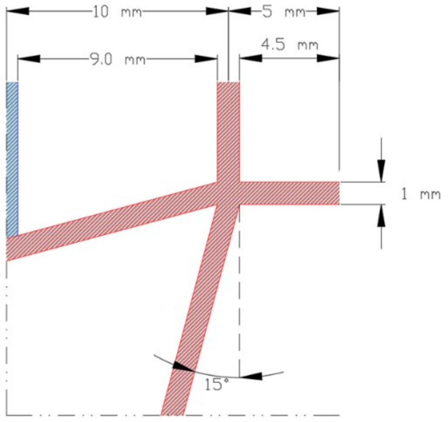

Figure C.7 Dimensions for a t=1mm 1/4 mesh.

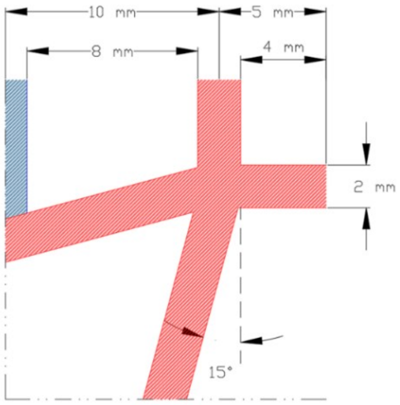

Figure C.8 Dimensions for a t=2mm 1/4 mesh.

# D

# Design of Experiments

L-PBF is a complex technique of manufacturing, as the equipment presents a wide selection of parameters and options that can affect the final product. To improve and correctly build a component, a parameter optimization needs to be performed. These parameters change due to several factors such as the material, the type of powders used, and the geometry of the piece. Thus, according to what has been exposed, a parameters optimization was carried out for each material used, specifically AlSi10Mg and Inconel 625.

To make sure the studied parameters are not only tuned for the material but also for the geometry, the samples were printed with the unit cell design in Figure 1.2.

## D.1 AlSi10Mg

### Parameters definition, production, and measurement

To do the design of this experiment, it was taken in consideration the results obtained by single tracks of AlSi10Mg with varying parameters from the thesis of Salgueiro, F. at ISQ produced in L-PBF with a Modulated Wave (MW). Accordingly, the study presented for Aluminum is not considered a DoE. A 3D object is nothing more than several single tracks together, layer by layer, making them the fundamental structural unit [35]. With that, considering the tracks in Figure D.9, the ones that presented continuity and uniformity were selected to be parameters to develop the experiments. It was also selected two set of parameters that did not presented uniformity namely samples 5 and 7, according to Table D.4 and a sample with the parameters suggested by the L-PBF for the material was also made.

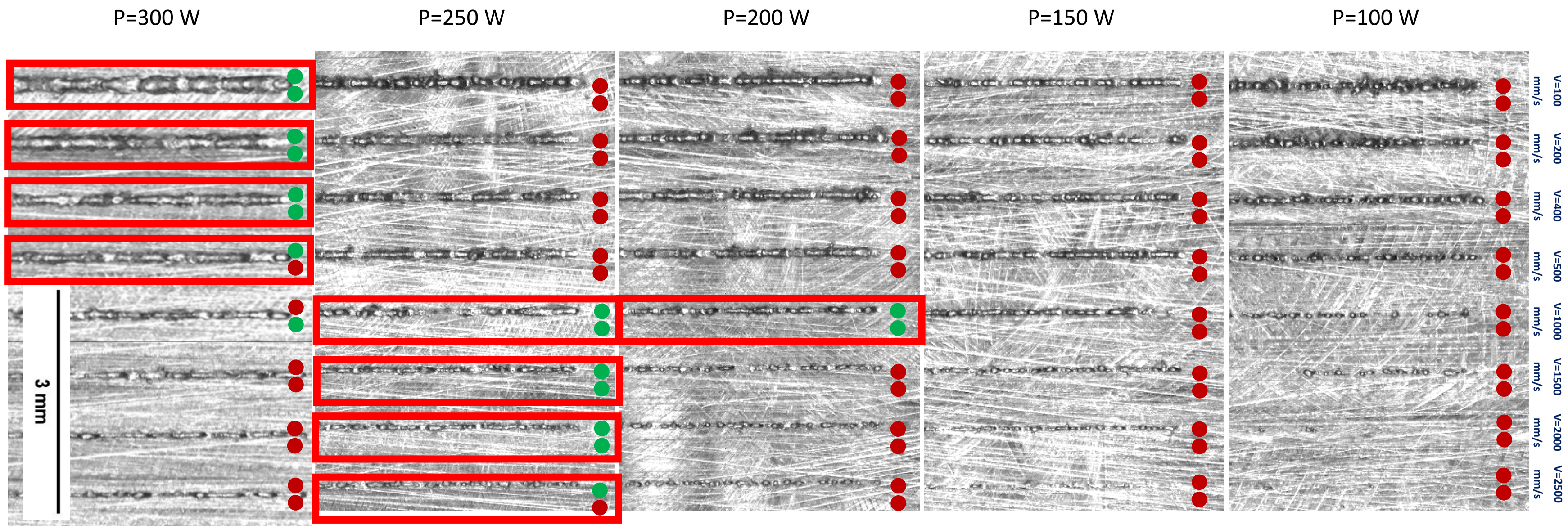

Figure D.9 Single tracks scanning study performed by Salgueiro, F.. The tracks whose parameters were used are signalled in red. The two dots in each track signal the continuity and the uniformity, respectively. (Adapted from Salgueiro, F. master thesis)

The first experiments planned are presented in Table D.4. All present a hatching distance of 90µm, an exposure time of 40µs and a layer thickness of 30µm. The volume energy deposition is provided by the laser beam and was calculated for each set. VED can be described by **Equation 1**, where P (W) is the laser power, L (mm) is the layer thickness, h(mm) is the hatching distance and v (mm/s) the velocity of the laser [62]. Since the samples were produced using laser with MW, the velocity of the laser is calculated by the ratio of point distance by exposure time.

**Equation 1**

$$VED\ [J \cdot mm^{-3}] = \frac{P\ [W]}{L\ [mm] \cdot h[mm] \cdot v[mm \cdot s^{-1}]}$$

Table D.4 First set of parameters defined for AlSi10Mg parameter optimization

| *Part ID* | *Power (W)* | *Velocity (mm/s)* | *Point Distance (µm)* | *VED (J/mm3)* |
|---:|---:|---:|---:|---:|
| *1* | 200 | 1000 | 40 | 74.1 |
| *2* | 250 | 1000 | 40 | 92.6 |
| *3* | 250 | 1500 | 60 | 61.7 |
| *4* | 250 | 2000 | 80 | 46.3 |
| *5* | 250 | 2500 | 100 | 37.0 |
| *6* | 300 | 100 | 4 | 1111.1 |
| *Not printed* | 300 | 200 | 8 | 555.6 |
| *8* | 300 | 400 | 16 | 277.8 |
| *9* | 300 | 500 | 20 | 222.2 |
| *7* | 350 | 2250 | 90 | 57.6 |

After preparing L-PBF for printing, the samples were printed in sets of 3 for each build plate. They were printed using supports of around 0,5 cm high. Some examples are shown in Figure D.10.

When printing samples 4, 5 and 6, due to a high VED, sample 6 in the first layer presented a balling phenomenon, as presented in Figure D .11, and the printing processes had to be stopped at that moment as it could be harmful for the re-coater. Since the sample "Not printed" had also a high VED, it was decided not to print to avoid that effect.

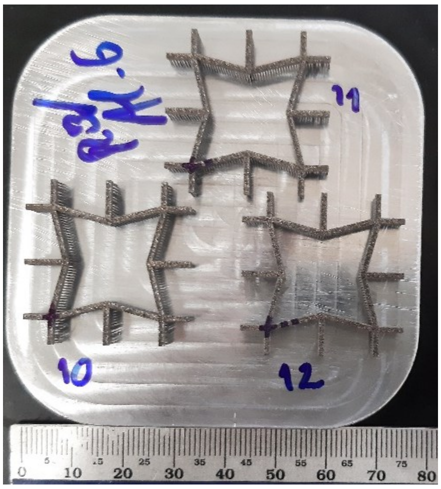

Figure D.10 Practical example of the samples 10, 11 and 12 for the parameters' optimization of AlSi10Mg.

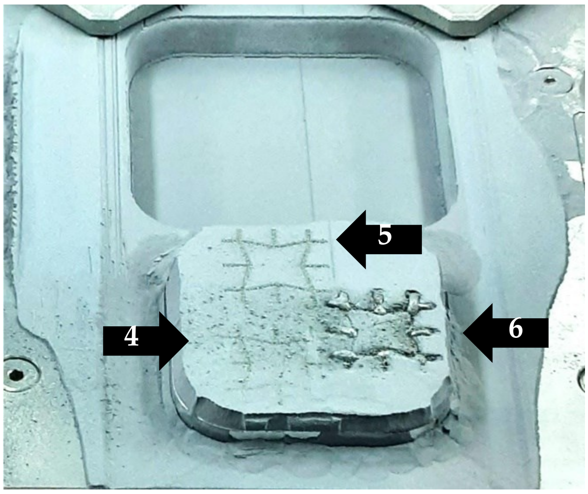

Figure D .11 Balling phenomenon during production of mesh sample 6.

The first measurements obtained were the thickness (t), taken with a micrometre in each knot of the mesh (8 measurements), and the width (w), with a Mitutoyo vernier calliper of each beam (12 measurements), according to the scheme presented in Figure D.12. The sample that corresponded to a t and w closer to 1, and with the lower standard deviation of both measurements, was sample 4 with a t of 1.178±0.029 mm and a w of 1.167±0.023 mm. The full table is presented in Table D.5, with all the responses measurements taken of each sample.

To optimize the set of parameters of the best sample, it was printed more 3 samples, varying the hatching distance to 120µm, 150µm and 180µm, as presented in Table D.6, keeping constant the ET of 40µs and a layer thickness of 30µm.

Table D.5 Data acquired for the parameter optimization of AlSi10Mg.

| Parameters | | | | | | | | | Measurements | | | | Surface roughness | | | Porosity | |
|---|---|---|---|---|---|---|---|---|---|---|---|---|---|---|---|---|---|
| Part ID | P (W) | v (mm/s) | PD (µm) | ET (µs) | v (m/s) | HD (mm) | LT (mm) | VED (J/mm3) | Average Thickness (mm) | Standard deviation (mm) | Average width (mm) | Standard deviation (mm) | Ra | Rq | Rz | BD | SD |
| 1 | 200 | 1000 | 40 | 40 | 1 | 0.090 | 0.03 | 74.1 | 1.372 | 0.016 | 1.208 | 0.036 | 8.525 | 10.557 | 40.596 | 1.630 | 0.562 |
| 2 | 250 | 1000 | 40 | 40 | 1 | 0.090 | 0.03 | 92.6 | 1.511 | 0.054 | 1.283 | 0.044 | 7.187 | 8.717 | 32.729 | 0.219 | 0.673 |
| 3 | 250 | 1500 | 60 | 40 | 1.5 | 0.090 | 0.03 | 61.7 | 1.301 | 0.009 | 1.229 | 0.024 | 9.724 | 12.323 | 45.989 | 0.203 | 3.028 |
| 4 | 250 | 2000 | 80 | 40 | 2 | 0.090 | 0.03 | 46.3 | 1.178 | 0.029 | 1.167 | 0.023 | Emb. | Emb. | Emb. | 0.335 | 0.305 |
| 5 | 250 | 2500 | 100 | 40 | 2.5 | 0.090 | 0.03 | 37.0 | 1.209 | 0.009 | 1.188 | 0.046 | 12.298 | 16.205 | 68.606 | 0.573 | 0.504 |
| 6 | 300 | 100 | 4 | 40 | 0.1 | 0.090 | 0.030 | 1111.1 | - | - | - | - | - | - | - | - | - |
| Not printed | 300 | 200 | 8 | 40 | 0.2 | 0.090 | 0.030 | 555.6 | - | - | - | - | - | - | - | - | - |
| 8 | 300 | 400 | 16 | 40 | 0.4 | 0.090 | 0.03 | 277.8 | 3.156 | 0.084 | 1.718 | 0.078 | 2.893 | 3.643 | 14.168 | 5.283 | 4.074 |
| 9 | 300 | 500 | 20 | 40 | 0.5 | 0.090 | 0.03 | 222.2 | 2.745 | 0.101 | 1.563 | 0.068 | 2.046 | 2.449 | 9.899 | 1.995 | 3.390 |
| 7 | 350 | 2250 | 90 | 40 | 2.25 | 0.090 | 0.03 | 57.6 | 1.273 | 0.020 | 1.166 | 0.046 | 7.765 | 9.424 | 36.342 | 0.127 | 0.189 |
| 10 | 250 | 2000 | 80 | 40 | 2 | 0.120 | 0.03 | 34.7 | 1.214 | 0.017 | 1.183 | 0.022 | 13.860 | 18.299 | 86.538 | 0.494 | 0.999 |
| 11 | 250 | 2000 | 80 | 40 | 2 | 0.150 | 0.03 | 27.8 | 1.198 | 0.014 | 1.160 | 0.024 | 14.261 | 17.148 | 72.299 | 2.795 | 2.826 |
| 12 | 250 | 2000 | 80 | 40 | 2 | 0.180 | 0.03 | 23.1 | 1.160 | 0.014 | 1.145 | 0.022 | Emb. | Emb. | Emb. | 7.970 | 7.534 |
| 13 | 300 | 500 | 20 | 40 | 0.5 | 0.120 | 0.03 | 166.7 | 2.308 | 0.045 | 1.486 | 0.047 | 2.631 | 3.158 | 13.122 | 4.925 | 5.097 |
| 14 | 300 | 500 | 20 | 40 | 0.5 | 0.150 | 0.03 | 133.3 | 1.979 | 0.073 | 1.403 | 0.058 | 4.624 | 5.576 | 24.595 | 3.390 | 4.323 |
| 15 | 300 | 500 | 20 | 40 | 0.5 | 0.120 | 0.06 | 83.3 | 1.989 | 0.035 | 1.457 | 0.059 | 1.953 | 2.521 | 9.834 | 2.789 | 2.230 |
| 16 | 300 | 500 | 20 | 40 | 0.5 | 0.150 | 0.06 | 66.7 | 1.804 | 0.026 | 1.350 | 0.034 | 5.075 | 6.578 | 25.692 | 5.411 | 5.755 |
| 17 | 300 | 500 | 20 | 40 | 0.5 | 0.180 | 0.06 | 55.6 | 1.624 | 0.029 | 1.336 | 0.045 | 6.170 | 8.476 | 35.179 | 1.749 | 2.481 |
| 18 | 250 | 2000 | 80 | 40 | 2 | 0.180 | 0.03 | 23.2 | 1.302 | 0.012 | 1.192 | 0.023 | Emb. | Emb. | Emb. | 6.486 | 0.323 |

Table D.6 Second set of parameters defined for the optimization of AlSi10Mg based on the parameters of sample 4, varying the hatching distance.

| *Part ID* | *Power (W)* | *Velocity (mm/s)* | *Hatching Distance (µm)* | *VED (J/mm3)* |
|---|---|---|---|---|
| ***4*** | ***250*** | ***2000*** | ***90*** | ***46.3*** |
| *10* | 250 | 2000 | 120 | 34.7 |
| *11* | 250 | 2000 | 150 | 27.8 |
| *12* | 250 | 2000 | 180 | 23.1 |

Since sample 9 had a smooth surface and best finish, in similarity with the before mentioned process, five more samples were printed, varying the hatching distance and the layer thickness, as presented in Table D.7.

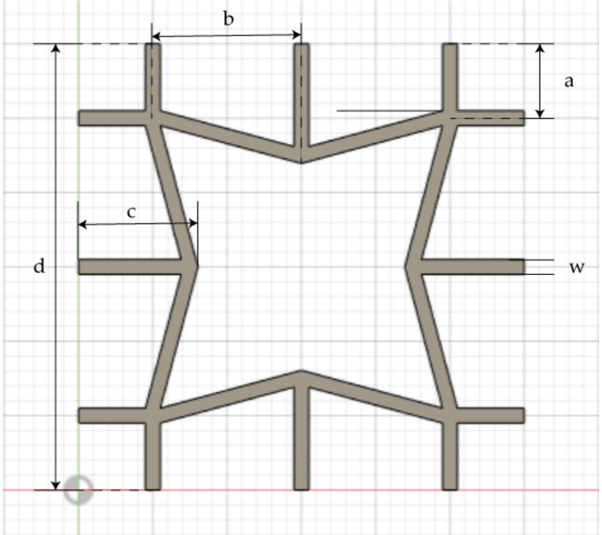

Figure D.12 Unit cell with the identification of measurements taken

Table D.7 Third set of parameters defined for the optimization of AlSi10Mg based on the parameters of sample 9, varying the hatching distance and layer thickness.

| *Part ID* | *Power (W)* | *Velocity (mm/s)* | *Hatching Distance (µm)* | *Layer thickness (µm)* | *VED (J/mm3)* |
|---|---|---|---|---|---|
| ***9*** | ***300*** | ***500*** | ***90*** | ***30*** | ***222.2*** |
| *13* | 300 | 500 | 120 | 30 | 166.7 |
| *14* | 300 | 500 | 150 | 30 | 133.3 |
| *15* | 300 | 500 | 120 | 60 | 83.3 |
| *16* | 300 | 500 | 150 | 60 | 66.7 |
| *17* | 300 | 500 | 180 | 60 | 55.6 |

Lastly, sample 4 and 12 were presenting the best values for t and w, so its parameters were chosen to produce an extra sample number 18 presented in Table D.8, using the same set of parameters of sample 12, adding the Renishaw's finish parameters. These parameters were mostly doble passages in the external area of each layer and in the total area of the first and last layer to promote unity and uniformity, as well a better surface finish. The 3 samples that presented the best values o t and w, are presented in Table D.8.

Table D.8 The samples presenting best t and w values for AlSi10Mg.

| *Part ID* | *Power (W)* | *Velocity (mm/s)* | *Hatching Distance (µm)* | *Layer thickness (µm)* | *VED (J/mm3)* |
|---|---|---|---|---|---|
| *4* | *250* | *2000* | *90* | *30* | *46.3* |
| *12* | *250* | *2000* | *180* | *30* | *23.1* |
| *18* | *250* | *2000* | *180* | *30* | *23.2* |

Every sample produced presented some warping, probably due to residual tensions and due to the methods of separation the samples from the build plates and supports.

During the printing process, no more measurements besides t and w had been taken. To accelerate the process the 3 best samples on those responses, presented in Table D.8, were selected and embedded in Epoxy resin to study the porosity, while the rest were still processing.

After the printing process was completed, each sample was measured using a vernier calliper and a micrometre, obtaining the "a", "b", "c" and "d" parameters, according to Figure D.12. The surface roughness was measured recurring to a mitutoyo surftest SJ-210. Since the 3 best samples were already embedded, they were not analysed for the rugosity and general measurements.

Every sample were broken in 2 or 3 parts, recurring to a plier, and subsequently embedded in Epoxy resin, recurring to a clincher, as represented in Figure D.13, to allow the analysis of the sample in the building direction, BD, or in scanning direction, SD. All samples were polished using EcoMet30 following the aluminium recipe (Annex A). They were observed under a Zeiss optical microscope with an Infinity 2 digital camera, whose images were analysed with ImageJ, obtaining the porosity in BD and SD, according to Figure D.14. The images taken are represented in Table D.12.

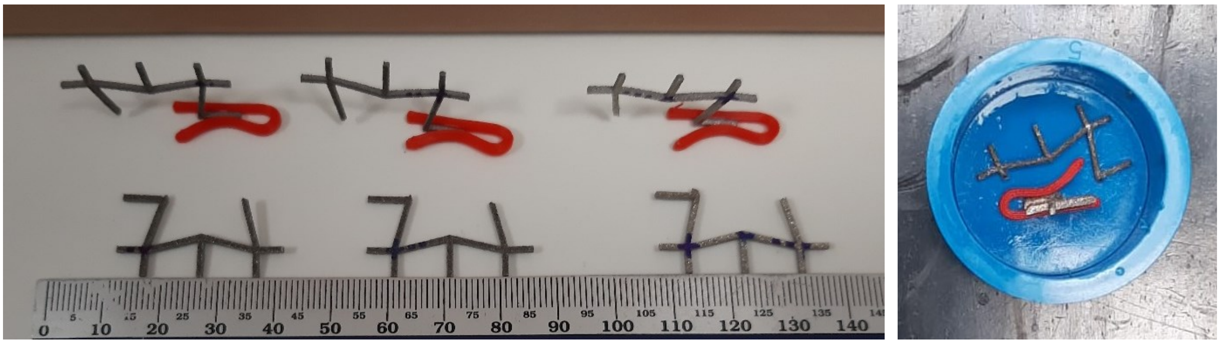

Figure D.13 Exemplification of how the samples were broken and positioned for embedment.

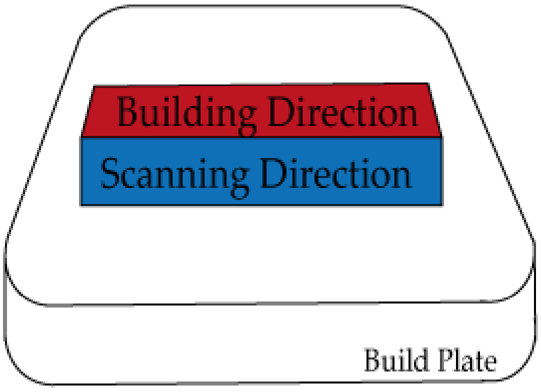

Figure D.14 Exemplification of the Scaning and Building direction in a rectangular piece

Table D.9 Composition of the microscopy images taken in BD and SD for the AlSi10Mg to obtain the porosity in each direction.

| | ***Scanning Direction*** | ***Building Direction*** |
|---|---|---|
| *Sample 1* | 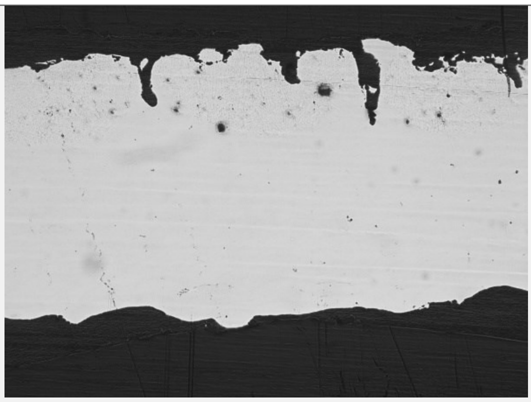 | 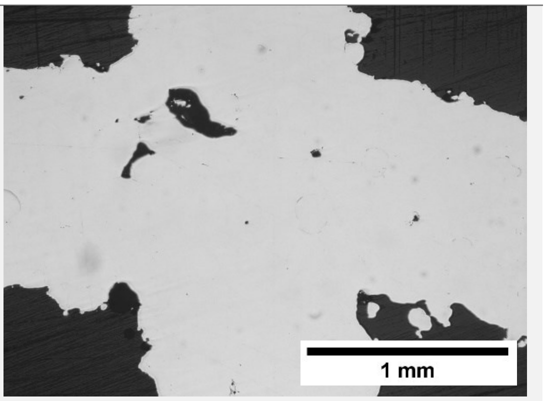 |

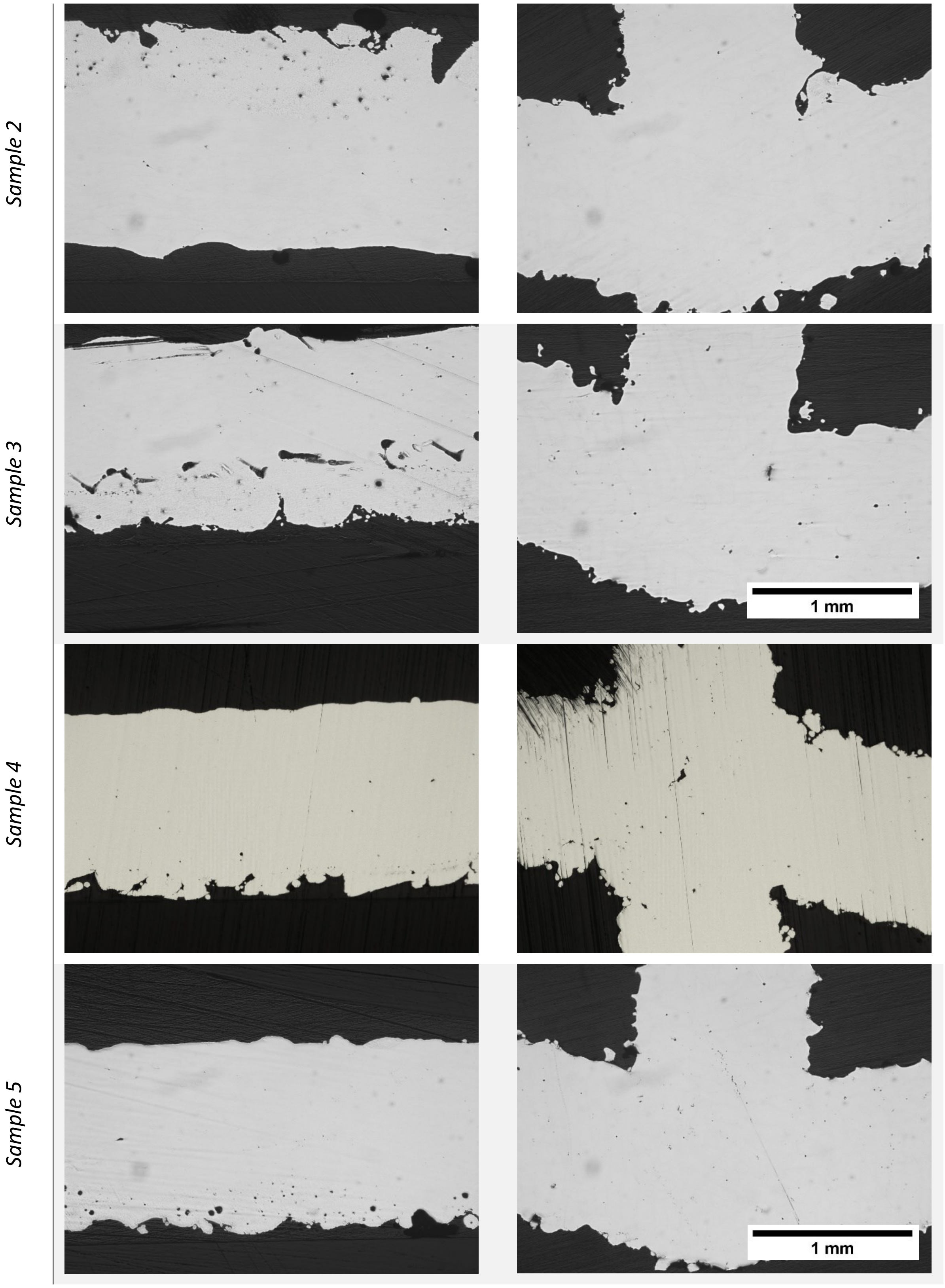
Sample 2
Sample 3
1 mm
Sample 4
Sample 5
1 mm

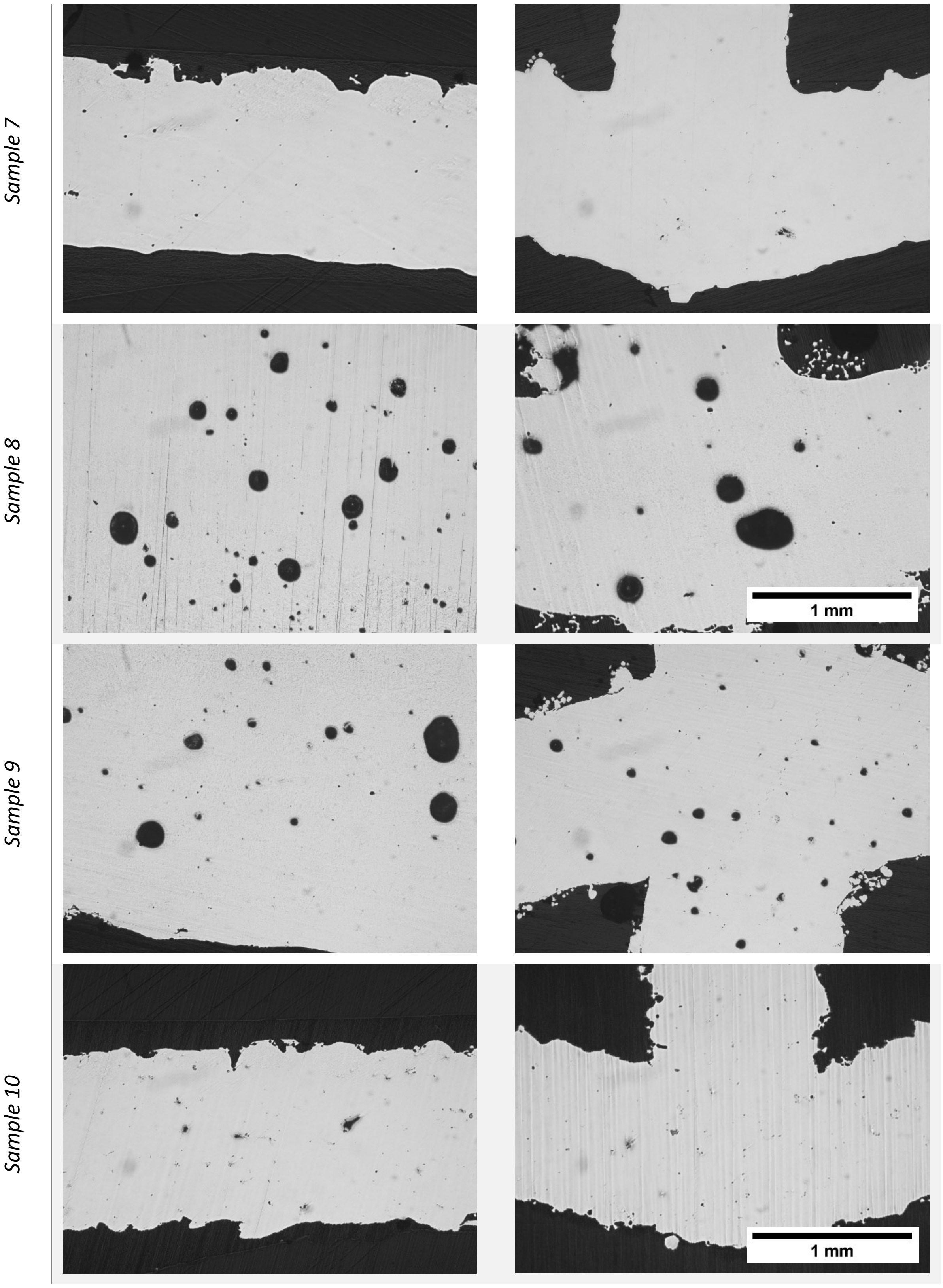
Sample 7
Sample 8
Sample 9
Sample 10
1 mm
1 mm

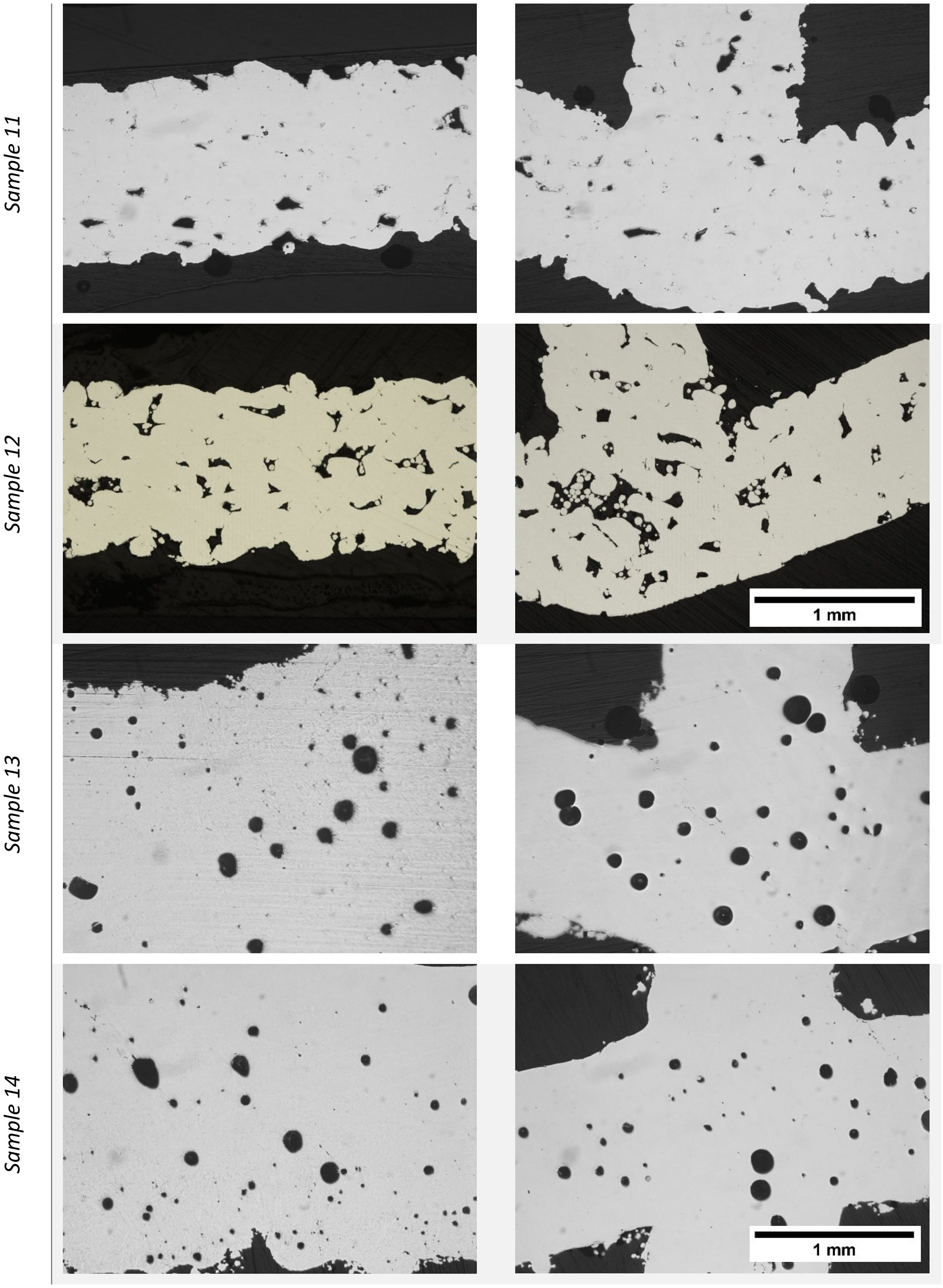
Sample 11
Sample 12
1 mm
Sample 13
Sample 14
1 mm

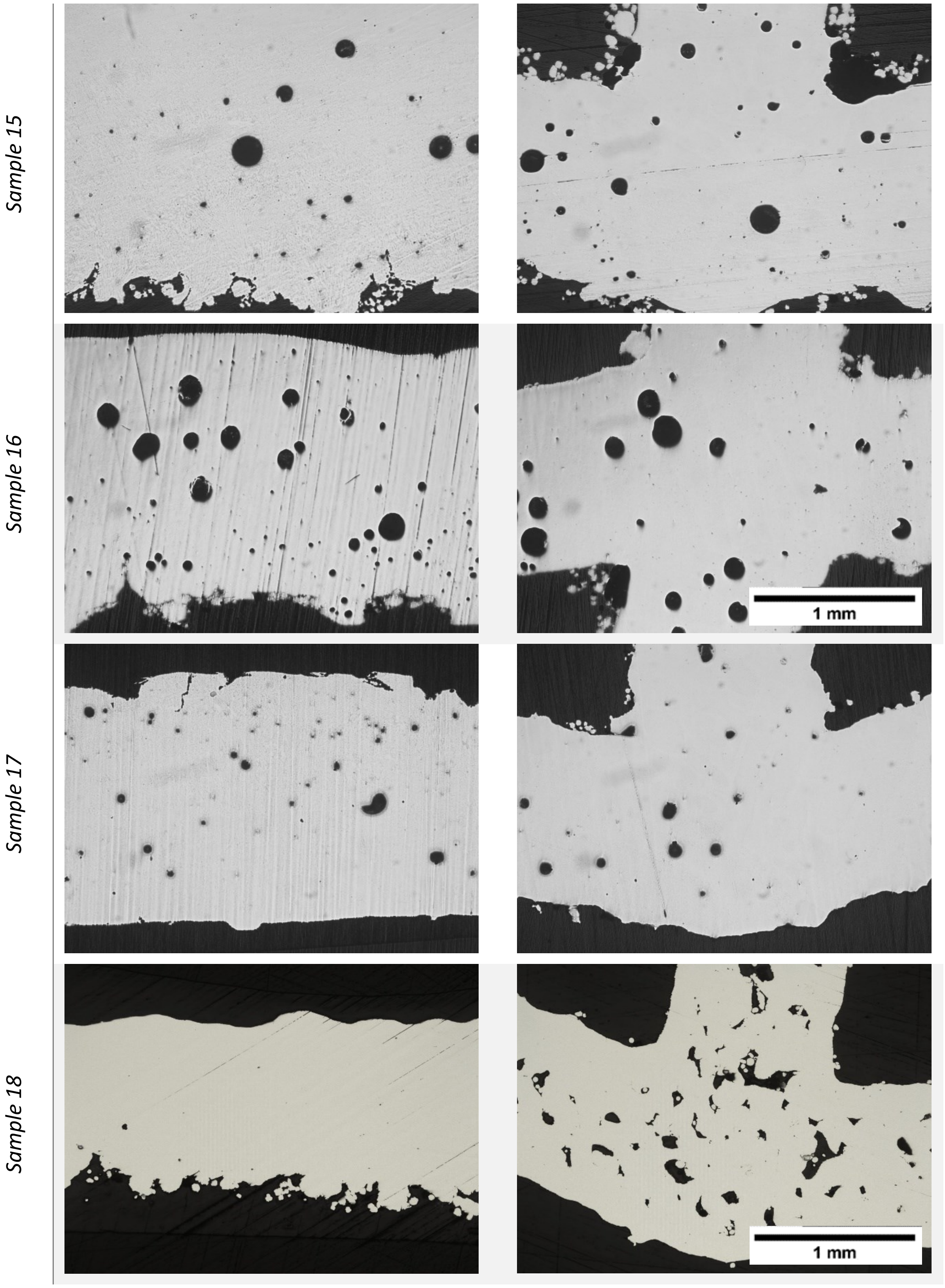
Sample 15
Sample 16
1 mm
Sample 17
Sample 18
1 mm

## Selection of the best set of responses

To choose the best set of parameters for the material in hand, the responses were compiled in a table, like Table D.10, and to each response a level was attributed according to each sample response order from smaller to larger. When the values were the same, an equal level was given. In the end the average of responses levels was calculated, where less the better. The smaller average was tied by sample 7 and 4. Sample 7 was chosen as the 1st option, since it had the smaller average of the response’s values.

Table D.10 Selection of the best samples, represented in bold. Tiebreakers are represented in red for 1st place and green for 3rd place.

| ***Sample*** | ***R1*** | ***Level*** | ***R2*** | ***Level*** | ***R3*** | ***Level*** | ***R4*** | ***Level*** | ***R5*** | ***Level*** | ***R6*** | ***Level*** | ***R7*** | ***Level*** | ***Level Av.*** | ***Resp. av.*** |
|---|---|---|---|---|---|---|---|---|---|---|---|---|---|---|---|---|
| *1* | 1.208 | 8 | 0.036 | 5 | 1.372 | 9 | 0.016 | 4 | 1.630 | 7 | 0.562 | 5 | 8.525 | 10 | 7 | 1.907 |
| *2* | 1.283 | 10 | 0.044 | 6 | 1.511 | 10 | 0.054 | 11 | 0.219 | 3 | 0.673 | 6 | 7.187 | 8 | 8 | 1.567 |
| ***3*** | **1.229** | **9** | **0.024** | **3** | **1.301** | **7** | **0.009** | **1** | **0.203** | **2** | **3.028** | **11** | **9.724** | **11** | **6** | **2.217** |
| ***4*** | **1.167** | **4** | **0.023** | **2** | **1.178** | **2** | **0.029** | **8** | **0.335** | **4** | **0.305** | **2** | **15.688** | **15** | **5** | **2.675** |
| *5* | 1.188 | 6 | 0.046 | 8 | 1.209 | 4 | 0.009 | 1 | 0.573 | 6 | 0.504 | 4 | 12.298 | 12 | 6 | 2.261 |
| ***7*** | **1.166** | **3** | **0.046** | **8** | **1.273** | **6** | **0.020** | **6** | **0.127** | **1** | **0.189** | **1** | **7.765** | **9** | **5** | **1.512** |
| *8* | 1.718 | 17 | 0.078 | 13 | 3.156 | 17 | 0.084 | 13 | 5.283 | 14 | 4.074 | 13 | 2.893 | 4 | 13 | 2.469 |
| *9* | 1.563 | 16 | 0.068 | 12 | 2.745 | 16 | 0.101 | 14 | 1.995 | 9 | 3.390 | 12 | 2.046 | 2 | 12 | 1.701 |
| *10* | 1.183 | 5 | 0.022 | 1 | 1.214 | 5 | 0.017 | 5 | 0.494 | 5 | 0.999 | 7 | 13.860 | 13 | 6 | 2.541 |
| *11* | 1.160 | 2 | 0.024 | 3 | 1.198 | 3 | 0.014 | 3 | 2.795 | 11 | 2.826 | 10 | 14.261 | 14 | 7 | 3.183 |
| *12* | 1.145 | 1 | 0.022 | 1 | 1.160 | 1 | 0.014 | 3 | 7.970 | 17 | 7.534 | 17 | 21.905 | 17 | 8 | 5.679 |
| *13* | 1.486 | 15 | 0.047 | 9 | 2.308 | 15 | 0.045 | 10 | 4.925 | 13 | 5.097 | 15 | 2.631 | 3 | 11 | 2.363 |
| *14* | 1.403 | 13 | 0.058 | 10 | 1.979 | 13 | 0.073 | 12 | 3.390 | 12 | 4.323 | 14 | 4.624 | 5 | 11 | 2.264 |
| *15* | 1.457 | 14 | 0.059 | 11 | 1.989 | 14 | 0.035 | 9 | 2.789 | 10 | 2.230 | 8 | 1.953 | 1 | 10 | 1.502 |
| *16* | 1.350 | 12 | 0.034 | 4 | 1.804 | 12 | 0.026 | 7 | 5.411 | 15 | 5.755 | 16 | 5.075 | 6 | 10 | 2.779 |
| *17* | 1.336 | 11 | 0.045 | 7 | 1.624 | 11 | 0.029 | 8 | 1.749 | 8 | 2.481 | 9 | 6.170 | 7 | 9 | 1.919 |
| *18* | 1.192 | 7 | 0.023 | 2 | 1.302 | 8 | 0.012 | 2 | 6.486 | 16 | 0.323 | 3 | 18.378 | 16 | 8 | 3.959 |

**Legend:** R1: Average width; R2: Average width deviation; R3: Average thickness; R4: Average thickness deviation; R5: Porosity in BD; R6: Porosity in SD; R7: Average surface roughness.

## D.2 Inconel 625

### Parameters definition

For the Design of Experiments of Inconel 625, in similarity of the parameter's optimization of AlSi10Mg, five different responses were chosen to optimize the parameters, namely the average thickness, the average width, the average surface roughness, the porosity in the building direction and the porosity in the scanning direction.

The controllable factors considered defined were power, velocity, and hatching distance, each with 3 levels as represented in Table D.11. For the DoE, 27 experiments were designed, classifying it as a full factorial represented by $3^3$. The elaborated correspondent design is available in Table D.15.

Table D.11 Parameters for the design of experiments of Inconel 625.

| *Level\Factors* | *Power [W]* | *Velocity [mm/s]* | *Hatching Distance [mm]* |
|---|---|---|---|
| *Low* | 100 | 500 | 0.08 |
| *Medium* | 200 | 1000 | 0.10 |
| *High* | 300 | 1500 | 0.12 |

Table D.12 Elaborated design for Inconel, with 27 samples, varying power, velocity and hatching distance.

| *Part ID* | *P (W)* | *v (mm/s)* | *Hatching Distance (µm)* |
|---|---|---|---|
| *1* | 100 | 500 | 80 |
| *2* | 100 | 500 | 100 |
| *4* | 100 | 500 | 120 |
| *5* | 100 | 1000 | 80 |
| *6* | 100 | 1000 | 100 |
| *13* | 100 | 1000 | 120 |
| *14* | 100 | 1500 | 80 |
| *7* | 100 | 1500 | 100 |
| *8* | 100 | 1500 | 120 |
| *10* | 200 | 500 | 80 |
| *11* | 200 | 500 | 100 |
| *12* | 200 | 500 | 120 |
| *16* | 200 | 1000 | 80 |
| *15* | 200 | 1000 | 100 |
| *17* | 200 | 1000 | 120 |

| | | | |
|---|---|---|---|
| ***18*** | 200 | 1500 | 80 |
| *19* | 200 | 1500 | 100 |
| *20* | 200 | 1500 | 120 |
| *9* | 300 | 500 | 80 |
| *21* | 300 | 500 | 100 |
| *22* | 300 | 500 | 120 |
| *23* | 300 | 1000 | 80 |
| *24* | 300 | 1000 | 100 |
| *25* | 300 | 1000 | 120 |
| *26* | 300 | 1500 | 80 |
| *27* | 300 | 1500 | 100 |
| *28* | 300 | 1500 | 120 |
| *3* | 375 | 1500 | 90 |

L-PBF is a high precision equipment, and its manufacturing variability is small when using the same printing conditions. The production of parts by this AM method, comes with elevated costs. Additionally, it was favored the production of a wide variety of samples with different parameters, thus in the present Design of Experiences, no replicas were planned.

## Experiments production and response measurement

The experiments were produced, without any other defect besides the warping that was also verified.

The responses were measured as described throughout AlSi10Mg, Parameters definition, production, and measurements chapter, and presented next, in Tables D.16 to D.22. In Table D.23 it is available the microscopy images taken in Building Direction and Scanning Direction, used for the measurement of the porosity in both direction of each sample.

Table D.13 Data acquired for the average thickness for each set of parameters

| | **Power, Watts (A)** | | | | | | | | |
|---|---|---|---|---|---|---|---|---|---|
| | **100** | | | **200** | | | **300** | | |
| **Hatching Distance, µm (C)** | **Velocity, mm/s (B)** | | | | | | | | |
| | **500** | **1000** | **1500** | **500** | **1000** | **1500** | **500** | **1000** | **1500** |
| **80** | 1.405 | 1.200 | 1.276 | 2.146 | 1.551 | 1.379 | 2.805 | 1.931 | 1.554 |
| **100** | 1.725 | 1.197 | 1.156 | 1.874 | 1.404 | 1.319 | 2.561 | 1.765 | 1.436 |
| **120** | 1.281 | 1.289 | 1.146 | 1.676 | 2.636 | 1.295 | 2.299 | 1.608 | 1.388 |

Table D.14 Data acquired for the thickness deviation for each set of parameters

| | Power, Watts (A) | | | | | | | | |
|---|---|---|---|---|---|---|---|---|---|
| | 100 | | | 200 | | | 300 | | |
| | Velocity, mm/s (B) | | | | | | | | |
| **Hatching Distance, µm (C)** | **500** | **1000** | **1500** | **500** | **1000** | **1500** | **500** | **1000** | **1500** |
| **80** | 0.026 | 0.024 | 0.038 | 0.037 | 0.018 | 0.034 | 0.040 | 0.026 | 0.022 |
| **100** | 0.030 | 0.023 | 0.018 | 0.030 | 0.039 | 0.029 | 0.085 | 0.038 | 0.013 |
| **120** | 0.013 | 0.037 | 0.035 | 0.025 | 3.537 | 0.032 | 0.036 | 0.060 | 0.040 |

Table D.15 Data acquired for the average width for each set of parameters

| | Power, Watts (A) | | | | | | | | |
|---|---|---|---|---|---|---|---|---|---|
| | 100 | | | 200 | | | 300 | | |
| | Velocity, mm/s (B) | | | | | | | | |
| **Hatching Distance, µm (C)** | **500** | **1000** | **1500** | **500** | **1000** | **1500** | **500** | **1000** | **1500** |
| **80** | 1.148 | 1.116 | 1.080 | 1.251 | 1.153 | 1.121 | 1.336 | 1.229 | 1.188 |
| **100** | 1.275 | 1.098 | 1.100 | 1.241 | 1.147 | 1.133 | 1.323 | 1.230 | 1.217 |
| **120** | 1.124 | 1.123 | 1.082 | 1.231 | 1.143 | 1.127 | 1.298 | 1.224 | 1.225 |

Table D.16 Data acquired for the width deviation for each set of parameters

| | Power, Watts (A) | | | | | | | | |
|---|---|---|---|---|---|---|---|---|---|
| | 100 | | | 200 | | | 300 | | |
| | Velocity, mm/s (B) | | | | | | | | |
| **Hatching Distance, µm (C)** | **500** | **1000** | **1500** | **500** | **1000** | **1500** | **500** | **1000** | **1500** |
| **80** | 0.007 | 0.018 | 0.027 | 0.023 | 0.030 | 0.026 | 0.053 | 0.031 | 0.020 |
| **100** | 0.040 | 0.018 | 0.020 | 0.027 | 0.038 | 0.043 | 0.104 | 0.038 | 0.033 |
| **120** | 0.036 | 0.059 | 0.019 | 0.038 | 0.034 | 0.049 | 0.058 | 0.035 | 0.034 |

Table D.17 Data acquired for the average roughness for each set of parameters

| | Power, Watts (A) | | | | | | | | |
|---|---|---|---|---|---|---|---|---|---|
| | 100 | | | 200 | | | 300 | | |
| | Velocity, mm/s (B) | | | | | | | | |
| **Hatching Distance, µm (C)** | **500** | **1000** | **1500** | **500** | **1000** | **1500** | **500** | **1000** | **1500** |
| **80** | 4.946 | 12.870 | 15.541 | 2.841 | 4.087 | 6.579 | 2.131 | 1.590 | 12.787 |
| **100** | 1.702 | 10.180 | 16.283 | 2.088 | 4.132 | 10.065 | 1.368 | 2.781 | 13.916 |
| **120** | 8.953 | 14.496 | 16.407 | 11.189 | 6.909 | 13.165 | 6.392 | 3.800 | 9.922 |

Table D.18 Data acquired for the porosity in building direction. for each set of parameters

| **Hatching Distance, µm (C)** | **Power, Watts (A)** | | | | | | | | |
|---|---|---|---|---|---|---|---|---|---|
| | **100** | | | **200** | | | **300** | | |
| | **Velocity, mm/s (B)** | | | | | | | | |
| | **500** | **1000** | **1500** | **500** | **1000** | **1500** | **500** | **1000** | **1500** |
| **80** | 0.151 | 2.748 | 13.260 | 2.157 | 0.063 | 0.072 | 1.088 | 0.064 | 0.040 |
| **100** | 0.082 | 6.839 | 14.331 | 0.385 | 0.055 | 0.475 | 0.321 | 0.069 | 0.165 |
| **120** | 0.259 | 10.353 | 18.970 | 0.067 | 0.042 | 1.638 | 1.930 | 0.260 | 0.246 |

Table D.19 Data acquired for the porosity in scanning direction for each set of parameters

| **Hatching Distance. µm (C)** | **Power, Watts (A)** | | | | | | | | |
|---|---|---|---|---|---|---|---|---|---|
| | **100** | | | **200** | | | **300** | | |
| | **Velocity, mm/s (B)** | | | | | | | | |
| | **500** | **1000** | **1500** | **500** | **1000** | **1500** | **500** | **1000** | **1500** |
| **80** | 0.267 | 4.039 | 3.700 | 2.168 | 4.490 | 1.491 | 4.773 | 3.486 | 0.074 |
| **100** | 0.054 | 6.590 | 17.099 | 2.795 | 7.930 | 0.172 | 1.489 | 0.022 | 0.135 |
| **120** | 0.483 | 9.264 | 15.185 | 4.294 | 1.352 | 1.350 | 0.033 | 0.118 | 0.378 |

Table D.20 Composition of the microscopy images taken in BD and SD for Inconel 625 to obtain the porosity in each direction.

| | ***Scanning Direction*** | ***Building Direction*** |
|---|---|---|
| *Sample 1* | 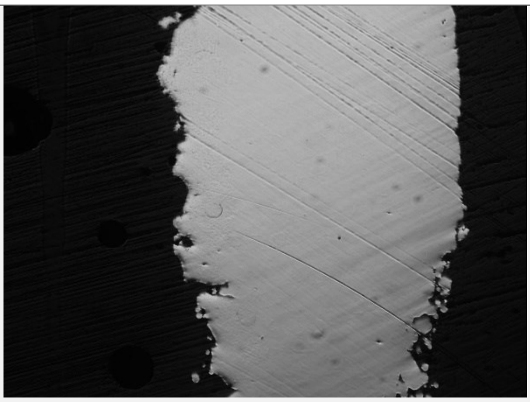 |  |
| *Sample 2* |  |  |
| *Sample 3* | 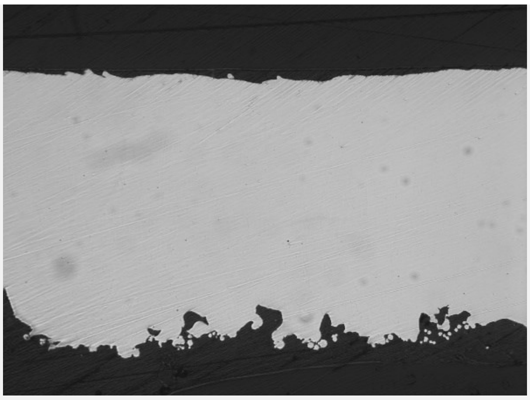 | 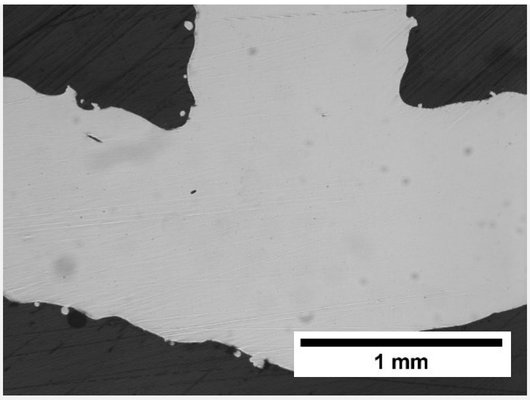 |

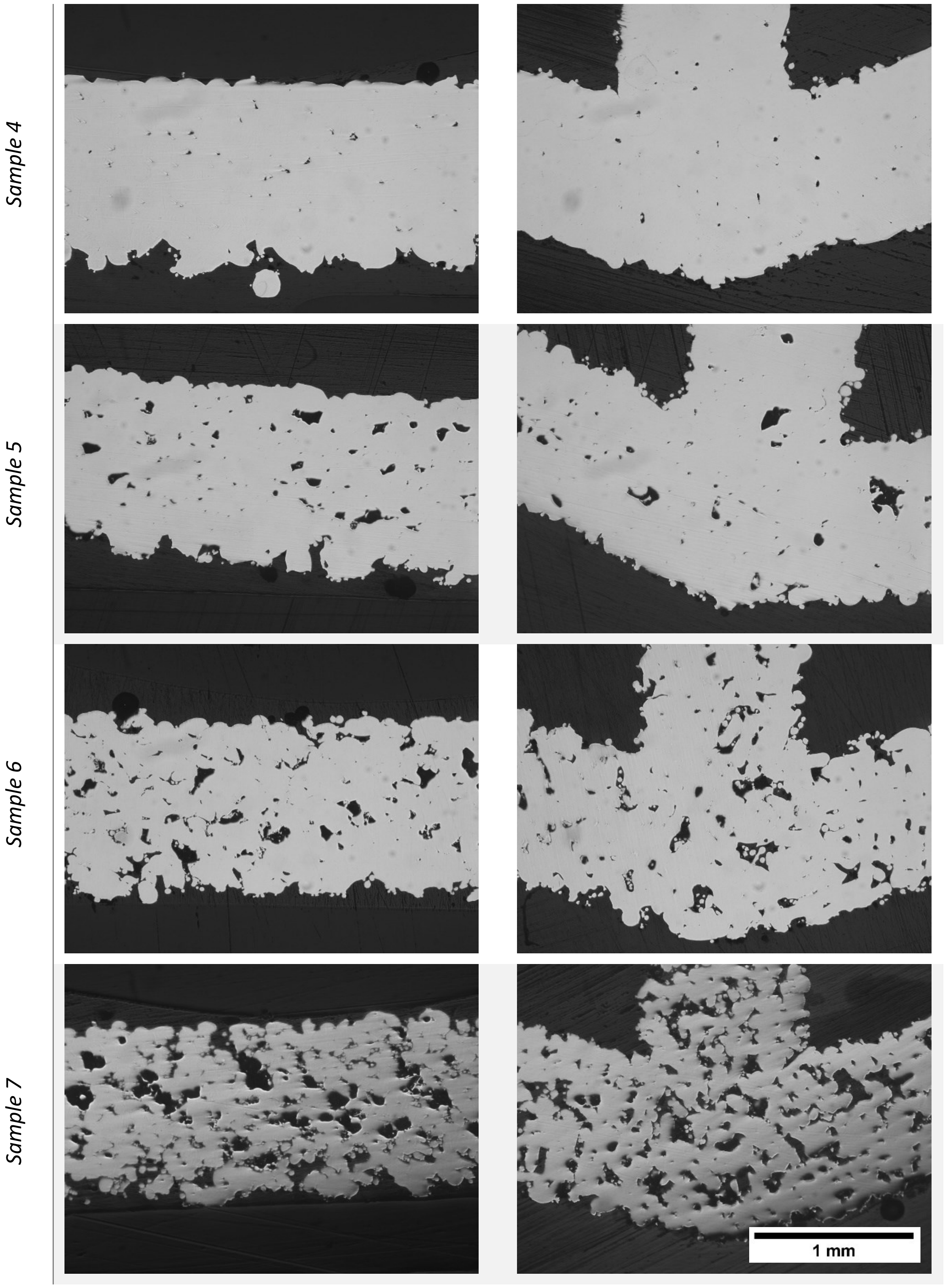
Sample 4
Sample 5
Sample 6
Sample 7
1 mm

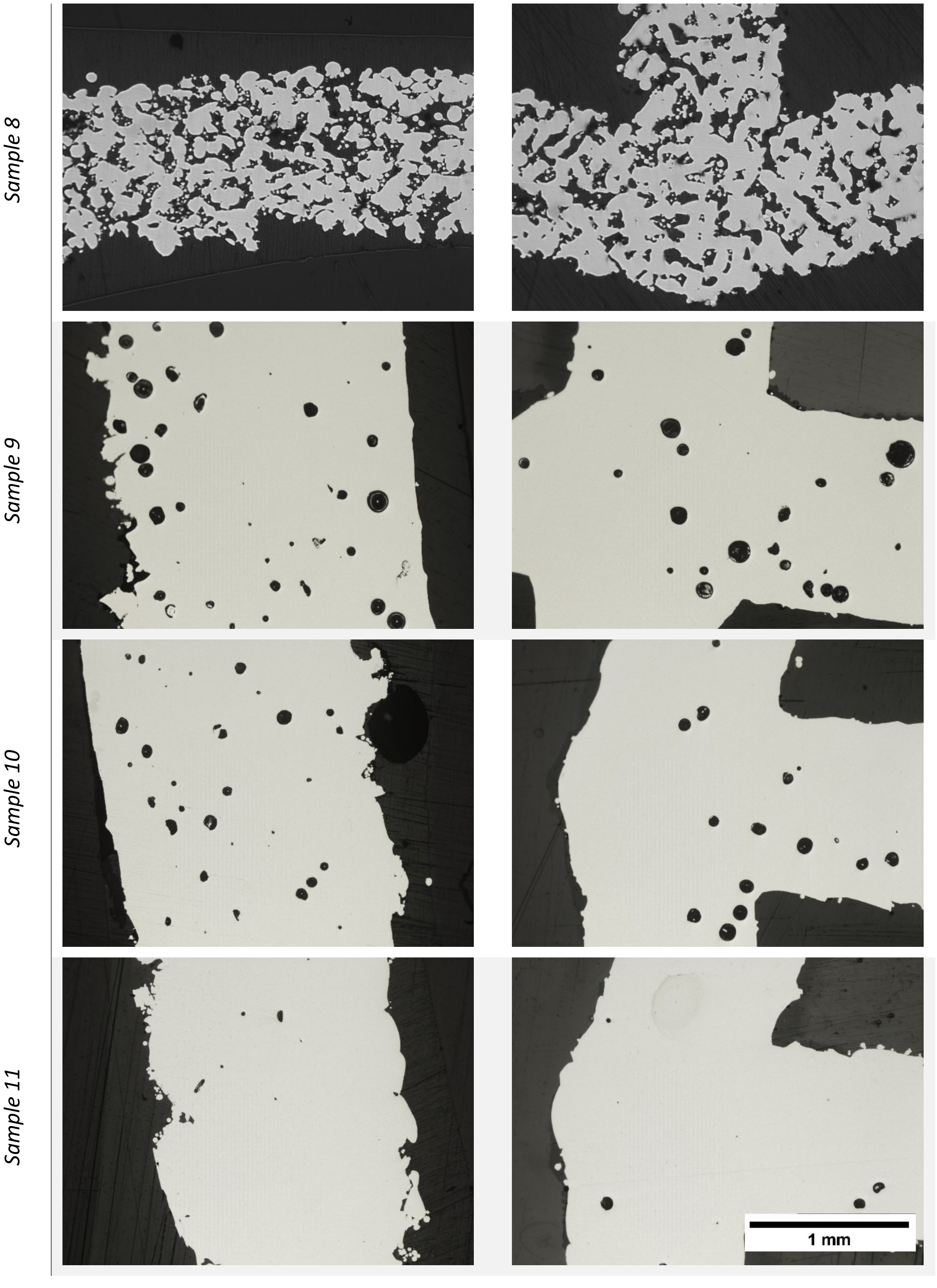
Sample 8
Sample 9
Sample 10
Sample 11
1 mm

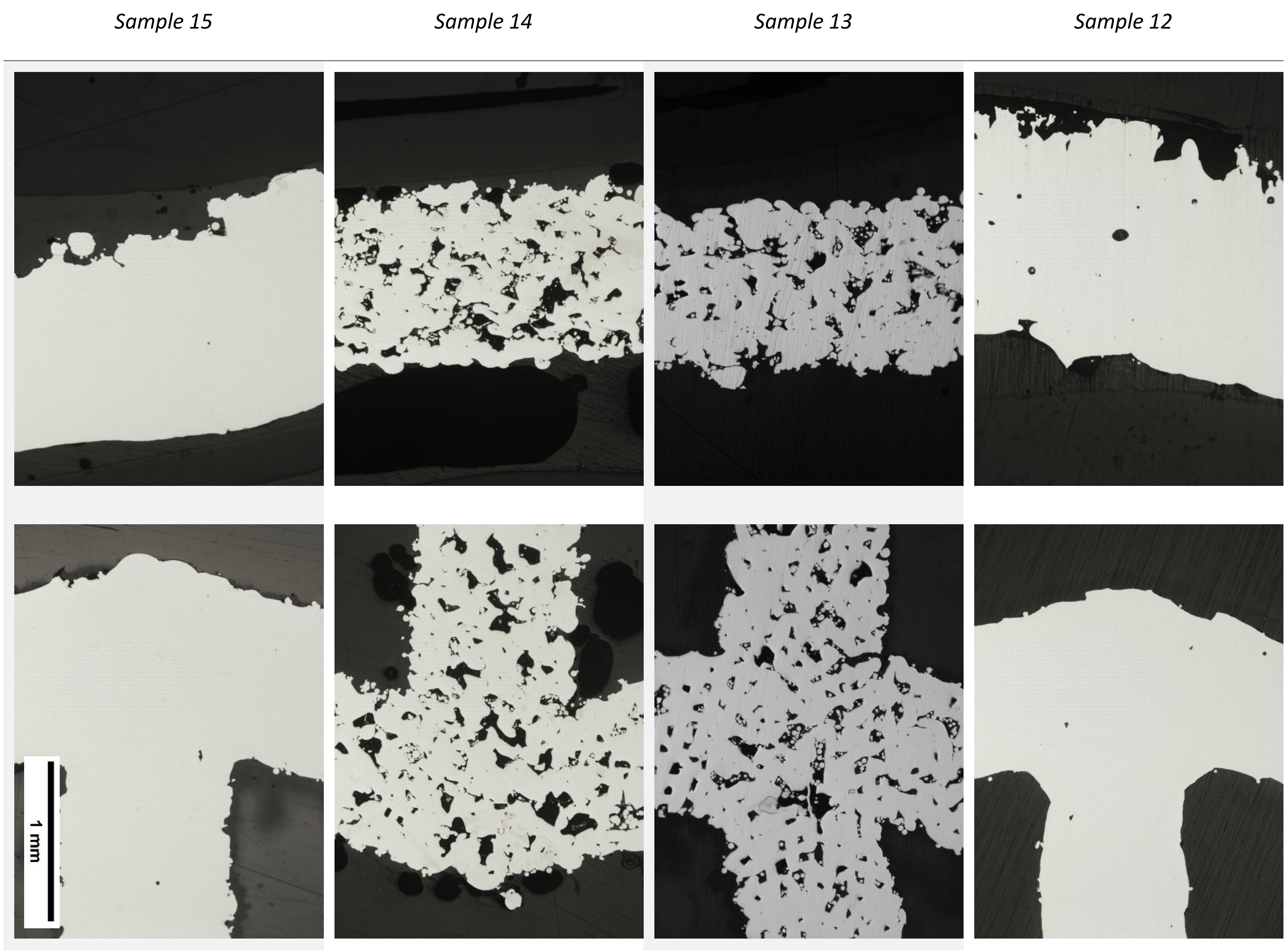
Sample 15
Sample 14
Sample 13
Sample 12
1 mm

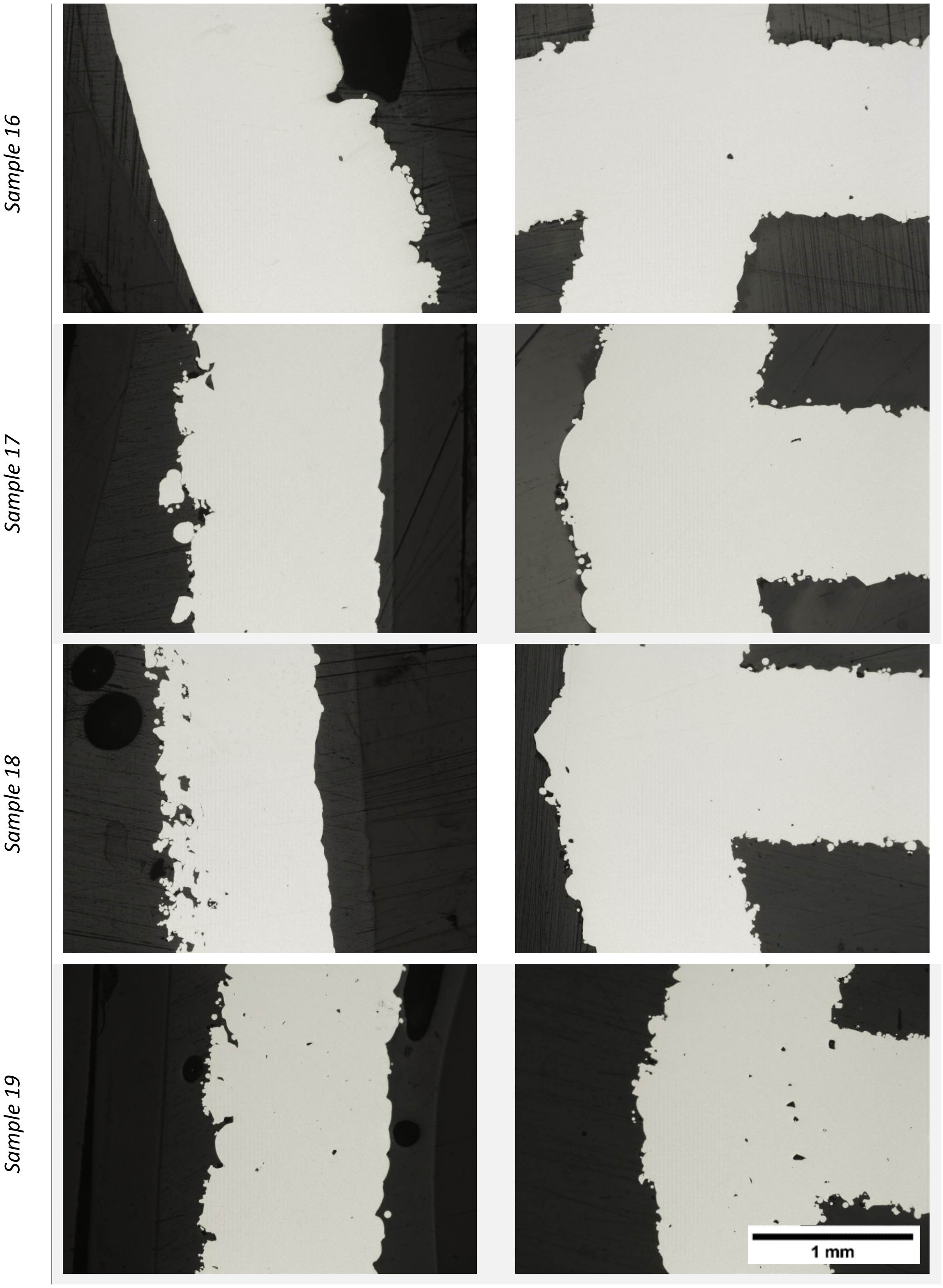
Sample 16
Sample 17
Sample 18
Sample 19
1 mm

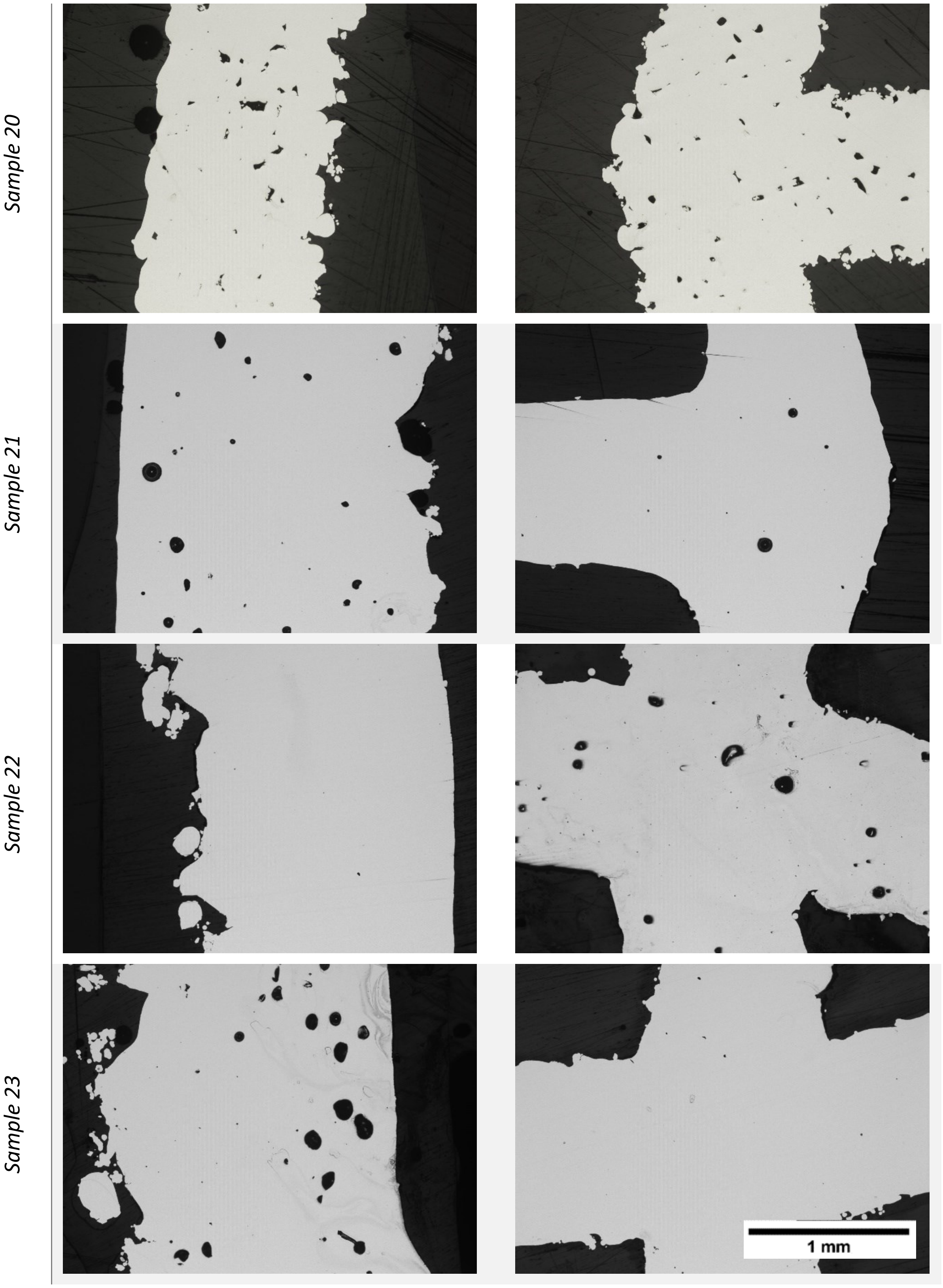
Sample 20
Sample 21
Sample 22
Sample 23
1 mm

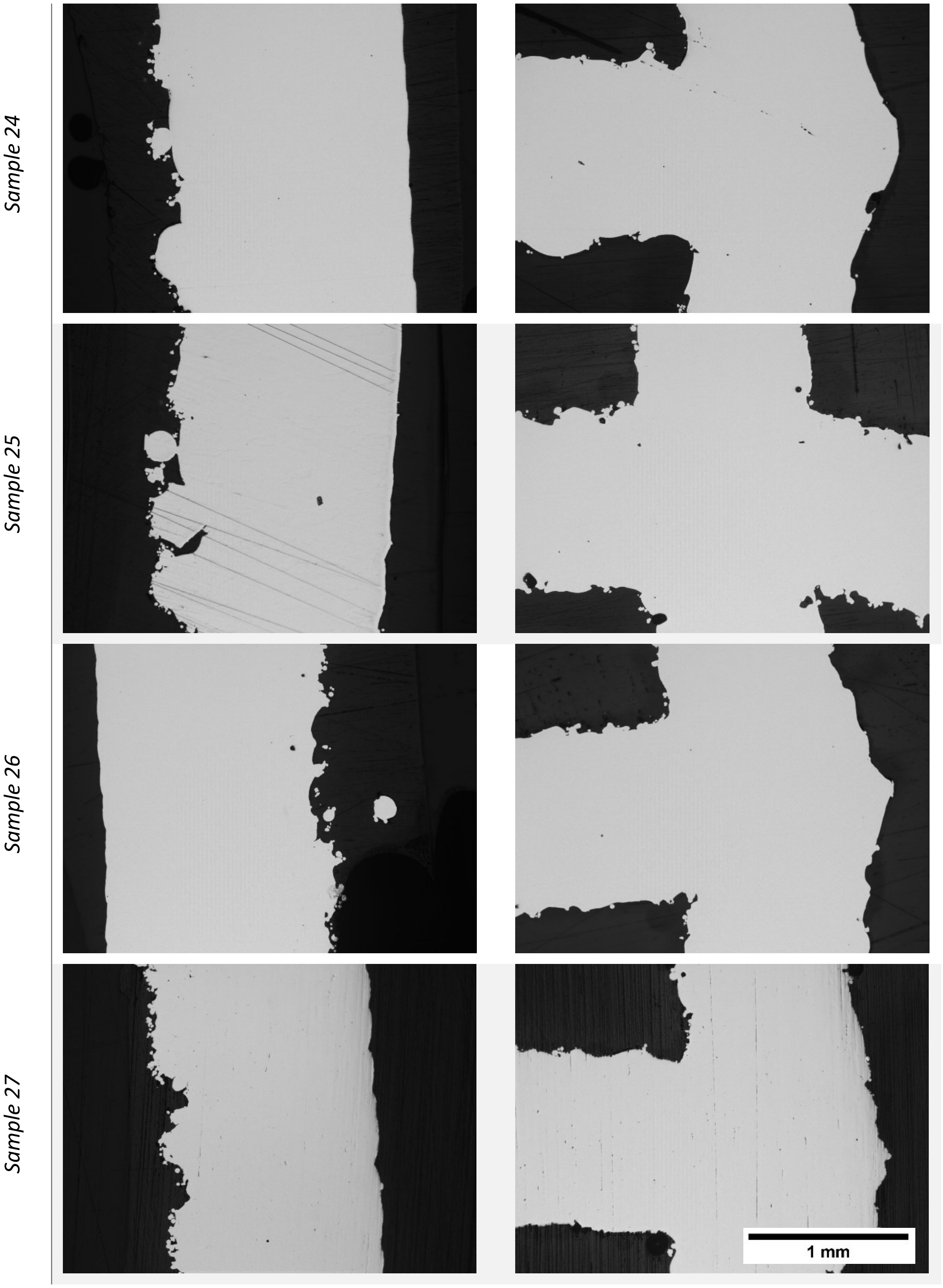
Sample 24
Sample 25
Sample 26
Sample 27
1 mm

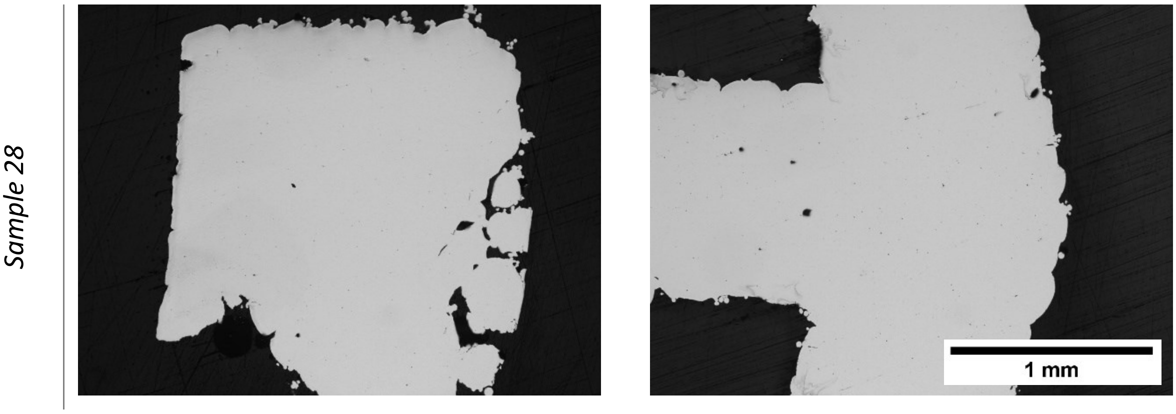

## Selection of the best set of responses

To analyze the acquired responses of all experiences, the Statistical Software Minitab was used.

In Minitab, the designed experiences parameters were inserted, as well as the correspondent five responses. Since the design was not made by the software, the factors and the type of the design had to be inputted. After that step, the responses were clarified, and the analysis was done automatically, giving us the analysis of variance for each response presented on Table D.24 to D.28, where it is possible to identify that the factors Power and Scanning speed are more significant than the hatching distance in every response.

Table D.21 Variance analysis for the average thickness

| ***Source*** | ***DF*** | ***Adj SS*** | ***Adj MS*** | ***F-Value*** | ***P-Value*** |
|---|---|---|---|---|---|
| *Model* | 18 | 5.308 | 0.295 | 4.54 | 0.017 |
| *Linear* | 6 | 3.761 | 0.627 | 9.64 | 0.003 |
| *Power (Watts)* | 2 | 1.831 | 0.916 | 14.09 | 0.002 |
| *Scanning Speed (mm/s)* | 2 | 1.890 | 0.945 | 14.54 | 0.002 |
| *Hatching Distance (µm)* | 2 | 0.04 | 0.020 | 0.31 | 0.743 |
| *2-Way Interactions* | 12 | 1.546 | 0.129 | 1.98 | 0.169 |
| *Power (Watts)*Scanning Speed (mm/s)* | 4 | 0.770 | 0.188 | 2.96 | 0.089 |
| *Power (Watts)*Hatching Distance (µm)* | 4 | 0.317 | 0.079 | 1.22 | 0.375 |
| *Scanning Speed (mm/s)*Hatching Distance (µm)* | 4 | 0.459 | 0.115 | 1.77 | 0.229 |
| *Error* | 8 | 0.520 | 0.065 | | |
| *Total* | 26 | 5.828 | | | |

Table D.22 Variance analysis for the average width

| ***Source*** | ***DF*** | ***Adj SS*** | ***Adj MS*** | ***F-Value*** | ***P-Value*** |
|---|---|---|---|---|---|
| *Model* | 18 | 0.138 | 0.008 | 9.14 | 0.002 |

| | | | | | |
|---|---|---|---|---|---|
| *Linear* | 6 | 0.131 | 0.022 | 25.97 | 0.000 |
| *Power (Watts)* | 2 | 0.072 | 0.036 | 42.90 | 0.000 |
| *Scanning Speed (mm/s)* | 2 | 0.057 | 0.028 | 33.78 | 0.000 |
| *Hatching Distance (µm)* | 2 | 0.002 | 0.001 | 1.24 | 0.340 |
| *2-Way Interactions* | 12 | 0.007 | 0.001 | 0.72 | 0.708 |
| *Power (Watts)*Scanning Speed (mm/s)* | 4 | 0.001 | 0.001 | 0.16 | 0.952 |
| *Power (Watts)*Hatching Distance (µm)* | 4 | 0.002 | 0.001 | 0.67 | 0.629 |
| *Scanning Speed (mm/s)*Hatching Distance (µm)* | 4 | 0.004 | 0.001 | 1.32 | 0.341 |
| *Error* | 8 | 0.007 | 0.001 | | |
| *Total* | 26 | 0.145 | | | |

Table D.23 Variance analysis for the roughness

| ***Source*** | ***DF*** | ***Adj SS*** | ***Adj MS*** | ***F-Value*** | ***P-Value*** |
|---|---|---|---|---|---|
| *Model* | 18 | 670.12 | 37.229 | 26.35 | 0.000 |
| *Linear* | 6 | 520.44 | 86.740 | 61.40 | 0.000 |
| *Power (Watts)* | 2 | 142.46 | 71.232 | 50.43 | 0.000 |
| *Scanning Speed (mm/s)* | 2 | 318.65 | 159.326 | 112.79 | 0.000 |
| *Hatching Distance (µm)* | 2 | 59.32 | 29.661 | 21.00 | 0.001 |
| *2-Way Interactions* | 12 | 149.68 | 12.474 | 8.83 | 0.002 |
| *Power (Watts)*Scanning Speed (mm/s)* | 4 | 80.43 | 20.107 | 14.23 | 0.001 |
| *Power (Watts)*Hatching Distance (µm)* | 4 | 26.55 | 6.637 | 4.70 | 0.030 |
| *Scanning Speed (mm/s)*Hatching Distance (µm)* | 4 | 42.71 | 10.677 | 7.56 | 0.008 |
| *Error* | 8 | 11.30 | 1.413 | | |
| *Total* | 26 | 681.42 | | | |

Table D.24 Variance analysis for the porosity in BD

| ***Source*** | ***DF*** | ***Adj SS*** | ***Adj MS*** | ***F-Value*** | ***P-Value*** |
|---|---|---|---|---|---|
| *Model* | 18 | 689.178 | 38.288 | 26.09 | 0.000 |
| *Linear* | 6 | 406.480 | 67.747 | 46.17 | 0.000 |
| *Power (Watts)* | 2 | 288.686 | 144.343 | 98.36 | 0.000 |
| *Scanning Speed (mm/s)* | 2 | 105.540 | 52.770 | 35.96 | 0.000 |
| *Hatching Distance (µm)* | 2 | 12.254 | 6.127 | 4.18 | 0.057 |
| *2-Way Interactions* | 12 | 282.698 | 23.558 | 16.05 | 0.000 |
| *Power (Watts)*Scanning Speed (mm/s)* | 4 | 254.079 | 63.519 | 43.28 | 0.000 |
| *Power (Watts)*Hatching Distance (µm)* | 4 | 19.288 | 4.822 | 3.29 | 0.071 |
| *Scanning Speed (mm/s)*Hatching Distance (µm)* | 4 | 9.332 | 2.333 | 1.59 | 0.267 |
| *Error* | 8 | 11.740 | 1.467 | | |
| *Total* | 26 | 700.918 | | | |

Table D.25 Variance analysis for the porosity in SD

| ***Source*** | ***DF*** | ***Adj SS*** | ***Adj MS*** | ***F-Value*** | ***P-Value*** |
|---|---|---|---|---|---|

| | | | | | |
|---|---|---|---|---|---|
| *Model* | 18 | 455.904 | 25.328 | 3.27 | 0.046 |
| *Linear* | 6 | 167.127 | 27.855 | 3.60 | 0.049 |
| *Power (Watts)* | 2 | 122.667 | 61.333 | 7.92 | 0.013 |
| *Scanning Speed (mm/s)* | 2 | 36.410 | 18.205 | 2.35 | 0.157 |
| *Hatching Distance (µm)* | 2 | 8.050 | 4.025 | 0.52 | 0.613 |
| *2-Way Interactions* | 12 | 288.777 | 24.065 | 3.11 | 0.058 |
| *Power (Watts)*Scanning Speed (mm/s)* | 4 | 195.258 | 48.814 | 6.31 | 0.014 |
| *Power (Watts)*Hatching Distance (µm)* | 4 | 66.008 | 16.502 | 2.13 | 0.168 |
| *Scanning Speed (mm/s)*Hatching Distance (µm)* | 4 | 27.512 | 6.878 | 0.89 | 0.513 |
| *Error* | 8 | 61.921 | 7.740 | | |
| *Total* | 26 | 517.826 | | | |

To do the optimization of responses, in the software was indicated that the goal is to minimize every response. In the case of the thickness and width, they were targeted for 1mm, which corresponds to the theoretical value. The parameters' goal and targets are represented in Table D.26

Table D.26 Responses goal and target for the optimization.

| *Response* | *Goal* | *Lower* | *Target* | *Upper* | *Weight* | *Importance* |
|---|---|---|---|---|---|---|
| *Porosity SD* | Minimum | - | 0.022 | 17.0990 | 1 | 1 |
| *Porosity BD* | Minimum | - | 0.040 | 18.9700 | 1 | 1 |
| *Roughness (µm)* | Minimum | - | 1.368 | 16.4070 | 1 | 1 |
| *Average width (µm)* | Target | 0.9 | 1.000 | 1.3358 | 1 | 1 |
| *Average thickness (µm)* | Target | 0.9 | 1.000 | 2.8049 | 1 | 1 |

The software, based on the goal inputted, automatically determines the optimal solution taking into consideration all the data. It was asked for it to give the top 3 results, being those presented in Table D.27. Analysing the table, the best solution has been achieved, specifically, sample number 18 parameters.

Table D.27 Optimized solutions given by the software Minitab.

| ***Solutions*** | | ***1st*** | ***2nd*** | ***3rd*** |
|---|---|---|---|---|
| *Sample number:* | | 18 | 1 | 15 |
| *Parameters* | *Power [W]* | 200 | 100 | 200 |
| | *Velocity [mm/s]* | 1500 | 500 | 1000 |
| | *Hatching distance [µm]* | 80 | 80 | 100 |
| *Fit* | *Porosity SD* | -1.084 | -2.044 | 5.455 |
| | *Porosity BD* | 0.570 | -0.840 | 0.147 |
| | *Roughness* | 7.550 | 4.728 | 3.721 |
| | *Average width* | 1.122 | 1.171 | 1.133 |
| | *Average thickness* | 1.347 | 1.557 | 1.570 |
| *Composite desirability* | | 0.783 | 0.766 | 0.750 |

2022 MARIANA MONTEIRO DUARTE ADDITIVE FABRICATION OF METALLIC ANEPECTIC MESHES

NOVA
NOVA SCHOOL OF
SCIENCE & TECHNOLOGY